July 2018

# Improvements to the UMASS S-Band FM-CW Vertical Wind Profiling Radar: System Performance and Data Analysis.

Joseph Waldinger

# IMPROVEMENTS TO THE UMASS S-BAND FM-CW VERTICAL WIND PROFILING RADAR: SYSTEM PERFORMANCE AND DATA ANALYSIS.

A Thesis Presented

by

JOSEPH WALDINGER

Submitted to the Graduate School of the
University of Massachusetts Amherst in partial fulfillment
of the requirements for the degree of

MASTER OF SCIENCE IN ELECTRICAL AND COMPUTER ENGINEERING

May, 2018

Electrical and Computer Engineering

# IMPROVEMENTS TO THE UMASS S-BAND FM-CW VERTICAL WIND PROFILING RADAR: SYSTEM PERFORMANCE AND DATA ANALYSIS.

A Thesis Presented

by

JOSEPH WALDINGER

Approved as to style and content by:

_____

Stephen Frasier, Chair

_____

Paul Siqueira, Member

_____

Ramakrishna Janaswamy, Member

_____

C.V. Hollot, Department Chair
Electrical and Computer Engineering

# DEDICATION

This is dedicated to those who choose to take on the role of mentor, and share their experience with others.

# ABSTRACT

## IMPROVEMENTS TO THE UMASS S-BAND FM-CW VERTICAL WIND PROFILING RADAR: SYSTEM PERFORMANCE AND DATA ANALYSIS.

MAY, 2018

JOSEPH WALDINGER

BS, NEW JERSEY INSTITUTE OF TECHNOLOGY

MS, UNIVERSITY OF MASSACHUSETTS AMHERST

Directed by: Professor Stephen Frasier

Upgrades to the University of Massachusetts S-Band FMCW boundary layer vertical wind profiling radar for use in the VORTEX-Southeast campaign are discussed. During the experiment, the radar characterizes velocity and reflectivity in clear-air and light to moderate precipitation conditions. Data is presented from the experiment which illustrates system performance and typical environmental results. This thesis begins with relevant background information on FM-CW radar operation, scattering mechanisms, and other calculations relevant to results discussed. The system hardware is described, along with improvements and modifications made prior to and during the experiment. Collected data is used to demonstrate system capabilities, improvements made, and remaining challenges. Various environmental features in the case of clear-air and precipitation are identified in the dataset. Several examples

of Drop Size Distribution (DSD) estimates are presented, and the possibility of separating vertical wind speed biases from rain data is explored. Finally, the validity of results of DSD estimates are discussed.

# TABLE OF CONTENTS

CHAPTER

# LIST OF FIGURES

# LIST OF TABLES

# CHAPTER 1

# INTRODUCTION



**Figure 1.1.** Picture of the UMass FMCW profiler at the 2016 deployment site during the Vortex Southeast experiment.

The Verification of the Origins of Rotation in Tornadoes Experiment - Southeast (VORTEX-SE) was conducted during March and April of 2016 and 2017 in the Huntsville, Alabama environs. The purpose of this experiment was to research storm development and to better characterize conditions which could support tornadogenesis in this region of the Southeast United States. VORTEX-SE was funded by the National Severe Storms Laboratory (NSSL).

Fine spatial scale measurement of vertical wind speed in this region is very useful for better characterization of the microstructure of storm development. Another parameter of interest to the experiment is measurement of the distribution of rain drop sizes. The UMass Frequency Modulated Continuous Wave (FM-CW) radar was deployed to constantly monitor vertical wind speeds and reflectivity in the Atmospheric Boundary Layer (ABL) throughout the experiment. The ABL constitutes the lowest atmospheric layer and can span a height of several kilometers.

The ability to continually monitor and report the state of the atmospheric boundary layer in real time is useful to the experiment. Fine-resolution characterization of vertical wind in the boundary layer is potentially useful in better understanding the atmospheric micro-structure during storm development in the region. Measurements of rain drop size distributions (DSDs) could also contribute towards a better understanding of local storm events.

FM-CW radars are unique in providing maximum duty cycle, allowing them to have high sensitivity for relatively low peak power requirements. This makes them useful in detecting weak signals, such as echo from clear-air. One challenge of FM-CW operation is the high dynamic range requirement. These systems utilize a simultaneous transmit and receive topology, and the power which leaks directly from the transmitter to receiver is typically a very large signal. Despite the benefits in sensitivity, there are few other FM-CW radars currently utilized as vertical wind profiling radars.

New technology in recent years has created higher performance capabilities in these systems [1]. Specifically, improved sampling and processing power associated with more powerful data acquisition systems allows higher sample rates and intensive real-time computations. In an FM-CW system, characteristics of the transmit signal and baseband sampling capabilities set nominal system parameters. Increased sam-

ple rate allows for improved measurement of velocity without compromising range resolution or maximum detectable range.

The UMass FMCW radar is an S-band vertical wind profiling radar. Figure 1.1 shows an image of the radar system from the VORTEX-SE campaign. Historically, it provided long-term monitoring of the refractive index structure parameter in the atmospheric boundary layer. In preparation for participation in VORTEX-SE, the radar underwent upgrades to the data acquisition system. The data acquisition hardware was replaced with a Software Defined Radio (SDR) to increase the baseband bandwidth. This allowed an increased velocity range such that the radar could measure not only clear-air velocities, but also rain drop velocities unambiguously. After upgrades, the system dynamic range is such that moderate rainfall would saturate the receiver but lighter rain events are fully characterizable.

Since the radar is vertically pointing, it can potentially estimate the (DSD). The drop size distribution can be estimated from the Doppler spectrum by assuming rain drops fall at their terminal velocity. Performing a change in parameters from the velocity to the drop size domain and normalizing the results yields the number density of rain drops per unit volume. Since this calculation depends on the assumption that rain drops fall at their terminal velocity, any bias in the vertical velocity will add error to the estimate. A correction can be applied during the DSD calculations to account for such known wind biases.

This thesis begins with background information on FM-CW radars, the radar range equation, and a discussion of rain rate estimation in Chapter 2. Chapter 3 details the hardware and modifications made before each deployment, as well as the data processing approach. The remaining chapters examine data collected during the experiment. Chapter 4 presents examples of collected data that reflect system performance. These examples specifically illustrate spurious products, noise, and other non-environmental artifacts which appear in the dataset. Examples of typical

clear-air environmental data are presented in Chapter 5. Chapter 6 discusses rain data, and details results of the drop size distribution estimates for several rain events. Finally, the attached appendix details specific and miscellaneous aspects of system operation and maintenance.

# CHAPTER 2

# BACKGROUND

## 2.1 FM-CW theory of operation

FM-CW radar systems work by simultaneously transmitting and receiving a frequency modulated waveform. This waveform is commonly a linear frequency modulation or chirp. The continuous-wave descriptor means the radar uses a waveform of high duty cycle; at or near 100%, as opposed to a conventional pulsed system. The benefit of such operation is that, at a 100% duty cycle, more energy is incident on scatterers than in a typical pulsed radar with the same peak power. The ability of a radar system to detect a target is a function of the energy incident on the target. Thus high sensitivity is more easily obtained in FM-CW radars. The costs include a trade-off in temporal resolution and the need for simultaneous transmission and reception. Simultaneous transmit and receive imposes a high dynamic range requirement on the receiver since a high power reflects from nearby ground clutter and leaks directly from the transmit antenna into the receive path [2].

An example of an ideal FM-CW system block diagram is shown in Figure 2.1. In this example a direct digital synthesizer is used to generate the frequency chirp. That chirp is upconverted to the radar frequency, fed into a high power amplifier (HPA), and then the antenna. The received signal is amplified and mixed with a signal coupled off the transmit chain. The resultant baseband signal can then be sampled and recorded.

The nature of the frequency-modulated waveform determines many system performance parameters. An example of two frequency modulated linear sweeps is given
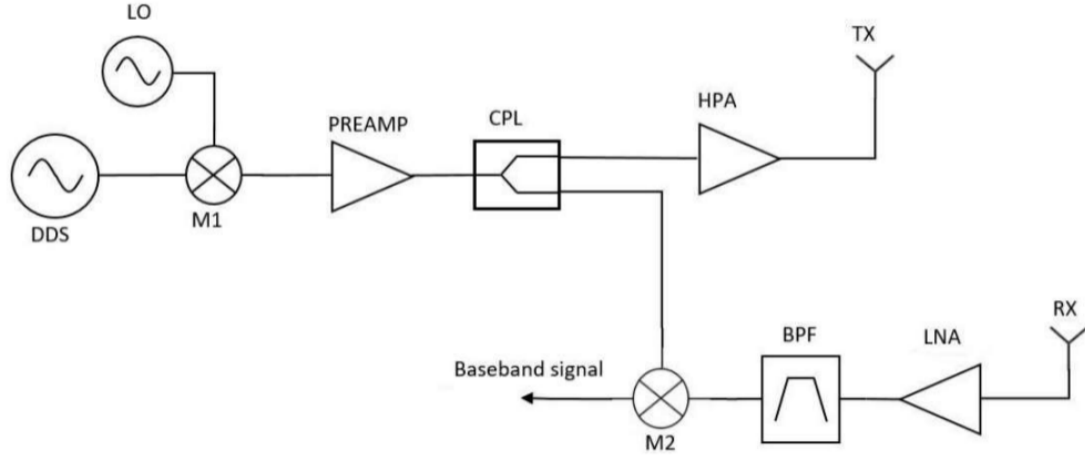
**Figure 2.1.** Simplified block diagram of a generic FM-CW system

in Figure 2.2a. Sweep time T is the time span of a single sweep, and bandwidth B is the difference between start and stop frequencies of the sweep. The chirp rate of the system is the slope of this line, given by $\dot{f} = \frac{B}{T}$. In this plot, the blue line represents a transmitted signal, and the green line a delayed and attenuated echo from a target. Figure 2.2b shows the waveform of the same linear chirp over a fraction of the sweep time, where the frequency is observed to increase with time and the signal magnitude remains constant.

The time delay between transmitting and receiving the echo from a target at range R is given by $\tau = \frac{2R}{c}$, where c is the speed of light. In the time it takes for an echo to reach the receiver, the transmitted signal will change frequency based on the chirp rate. The beat frequency obtained by mixing the echo chirp with the transmitted chirp is $f_B = \tau * \dot{f}$. This expands to $f_B = \frac{2R}{c}\frac{B}{T}$, thus echoes from different ranges exhibit different beat frequencies.

Range resolution and maximum range of the system can be found from the above equation for $f_B$. Solving for $\Delta R$ yields $\Delta R = \Delta f_B T \frac{c}{2B}$. Frequency resolution $\Delta f_B$ is approximately $\frac{1}{T}$ based on Fourier Transform properties. Range resolution thus reduces to, $\Delta R = \frac{c}{2B}$. Via the Nyquist Theorem, the highest baseband frequency which

6

(a) Frequency vs time

(b) Magnitude vs time
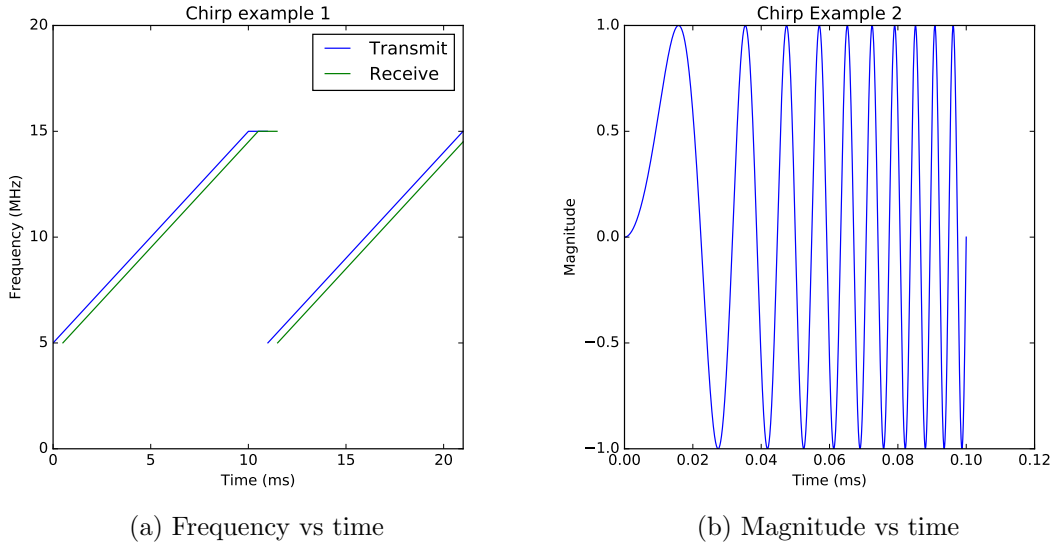
**Figure 2.2.** Example of a linear frequency chirp for a 10 MHz bandwidth and a 10 millisecond sweep time.

can be measured unambiguously is one half of the A/D sample rate, $\frac{f_s}{2}$. Combining this with the frequency-range relation discussed above, $\frac{f_s}{2} = \dot{f}\frac{2R_{max}}{c}$. Solving for the maximum range,

$$R_{max} = \frac{f_s c}{4\dot{f}} \tag{2.1}$$

Figure 2.3 shows a simulated baseband frequency spectrum from an FM-CW system observing a single target. The simulation uses the same frequency chirp as in Figure 2.2; a waveform with 10ms sweep time and 10MHz bandwidth. From the above equations, this system would have a chirp rate of 1 $\frac{GHz}{sec}$, and range resolution of 15 m. The theoretical target is set to a range of 10 km, corresponding to a 67 $\mu sec$ delay. The receiver is assumed to sample 2048 points per sweep at a 200 kHz sample rate leading to a maximum range of 15 km. The theoretical baseband signal is the result of multiplying the time-domain waveform by a copy delayed 67 $\mu sec$. A von Hann window is then applied to this baseband signal to reduce range sidelobes introduced by discontinuities at the sample range edges, and a Fourier Transform was

7
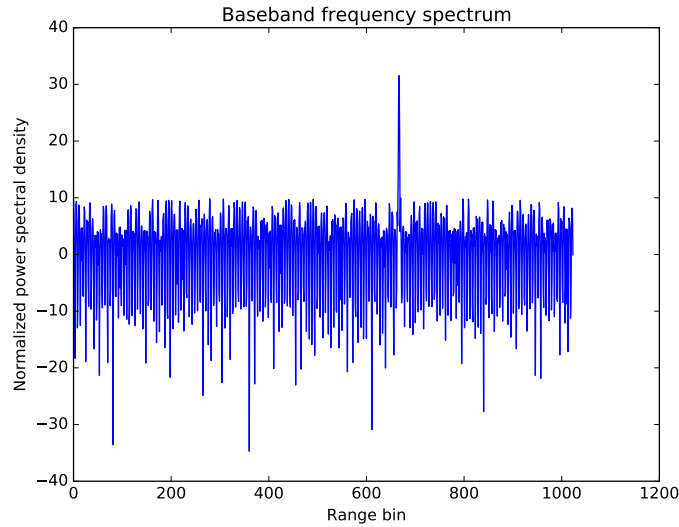
**Figure 2.3.** Simulated power spectral density of theoretical baseband signal, with a target at a range of 10 km.

performed. The Fourier Transform is then normalized to its average, and converted to a log scale. The simulated target appears in range bin 667; or at an apparent range of 10 km, as expected.

Once the radar baseband signal is converted from the single-sweep time-sample domain to the range domain, Doppler information can be extracted by comparing successive sweeps. By performing an additional Fourier Transform at each range bin over several sweeps, a Doppler Spectrum is obtained for each range bin. In this domain, Doppler frequency is given by $f_D = \frac{2u}{\lambda}$, where $u$ represents radial target velocity, and $\lambda$ the average radar wavelength. Maximum unambiguous velocity is given by $u_{max} = \frac{\lambda}{4T}$. This parameter is determined by the time between successive sweeps, assuming a constant system wavelength. The velocity resolution is set by the total velocity range, $2u_{max}$, divided by the number of sweeps used in the Fourier Transform.

## 2.2 Radar Range Equation

In general, the received power level detected by a radar from a target is given by the radar range equation,

$$P_r = \frac{P_t G_t G_r \lambda^2 \sigma}{(4\pi)^3 R^4} \tag{2.2}$$

Where $\sigma$ is the radar cross section, G represents antenna gain, and $P_t$ and $P_r$ represent the transmitted and received power, respectively.

In the case of volume scattering, the radar cross section must be expressed in terms of volume reflectivity $\eta$. The conversion in the case of a narrow antenna beam is given by $\sigma = \Delta R \frac{\pi}{4} \beta^2 R^2 \eta$, where $\beta$ is the antenna beam width in radians [3]. The Fourier transform and windowing functions applied to convert time to the range domain introduces gain term $G_c$ due to coherent integration, where $G_c = \frac{B_n * T}{4}$. The range equation in this case is given by,

$$P_r = \frac{P_t G_t G_r G_c \lambda^2 \beta^2 \Delta R}{4^4 \pi^2} \frac{\eta}{R^2} \tag{2.3}$$

The single sweep signal to noise ratio is given by $SNR_1 = \frac{P_r}{P_n}$, where $P_n$ represents the received noise power. This noise power is described by $P_n = kB_n(T_{rec} + T_A)$, where $T_A$ is the antenna temperature, $T_{rec}$ is the equivalent receiver temperature, $k$ is Boltzmann's constant, and $B_n$ represents the receiver noise bandwidth. The receiver temperature is a function of receiver noise factor $F$, where $T_{rec} = (F-1)T_0$. Antenna temperature can be approximated by $T_A = \eta_{rad} T_B + (1 - \eta_{rad}) T_P$, where $\eta_{rad}$ is the antenna's radiation efficiency, $T_P$ is the physical temperature of the antenna, and $T_B$ is the brightness temperature which the antenna sees. [4] Combining these with the above radar range equation,

$$SNR_1 = \frac{P_t G_t G_r G_c \lambda^2 \beta^2 \Delta R}{4^4 \pi^2 k B_n (T_{rec} + T_A)} \frac{\eta}{R^2} \tag{2.4}$$

9

## 2.3   Scattering Mechanisms

In the case of wind profiling of the atmospheric boundary layer, returns from clear-air signals are largely based on Bragg scattering from refractive index turbulent fluctuations. Reflections from air which is turbulent on the spatial scale of one half radar wavelength interfere constructively, causing sufficient power levels to be measured by the system. Refractive index differences driven by humidity gradients are the primary mechanism for scattering from these targets. The refractive index structure parameter $C_{n^2}$ is a metric which describes these fluctuations, and is related to volume reflectivity by (2.5). [5] [6]

$$\eta = 0.38\lambda^{-\frac{1}{3}}C_{n^2} \tag{2.5}$$

For Rayleigh scattering particles, such as precipitation, we define reflectivity factor $Z$ as related to $\eta$ as (2.6). $K$ is a function of the complex index of refraction; for rain, $|K|^2 \approx 0.9$. Rain drops scatter in the Rayleigh domain but other targets of interest do not. Regardless of the actual target scattering mechanism, this equation can be used to define an equivalent reflectivity factor,

$$\eta = \frac{\pi^5}{\lambda^4}|K|^2 Z \tag{2.6}$$

and in the case of precipitation, $Z$ is related to the drop size distribution as the sixth moment [7],

$$Z = \sum_{i=1}^{N} d_i^6. \tag{2.7}$$

Theoretical sensitivity is typically estimated as the received power corresponding to a single sweep SNR of 0dB. In other words, the minimum detectable signal is assumed to occur at the same power level as the noise power. Inverting (2.4), the volume reflectivity corresponding to each received power level is found as a function of the system parameters and theoretical noise temperature values. Using the structure

parameter relation previously discussed, the minimum detectable structure parameter which this system can detect is found,

$$C_{n^2,min} = \frac{4^4 \pi^2 k B (T_{rec} + T_A)}{0.38 P_t G^2 \lambda^{\frac{5}{3}} \beta^2 \Delta R} \qquad (2.8)$$

## 2.4 Theory of Rain Rate Estimation

Since this radar points vertically and employs full Doppler processing, it is theoretically possible to estimate the drop size distribution for rain events. By assuming rain drops fall near their terminal velocity, each velocity bin in the Doppler spectrum can be mapped to an equivalent drop size bin. This assumption is not true when there is vertical wind present, and sometimes a correction must be applied for accurate results. The governing relations to estimate DSDs initially detailed in Atlas (1973) [8] are summarized below.

The relation between terminal velocity and drop diameter for drop sizes between approximately 0.1 mm and 6 mm is given by,

$$v(D) = 9.65 - 10.3e^{-0.6D}, \ \textbf{for} \ 0.109 < D < 6 \qquad (2.9)$$

where $D$ represents drop diameter in millimeters.

For these calculations it is assumed that volume reflectivity $\eta(v)$ is known as a function of height and velocity. A change in variables from velocity to drop size is required, in which $\eta(D) = \eta(v)\frac{\partial v}{\partial D}$, where $\eta(D)$ represents volume reflectivity as a function of drop size. The term $\frac{\partial v}{\partial D}$ is found by differentiation of (2.9). It is worth noting that while velocity bins are uniform in size, drop-size bins are not.

This result can now be normalized to the drop size distribution $n(D)$ using $n(D) = \frac{\eta(D)}{\sigma(D)}$. Where $\sigma(D)$ represents the single particle backscatter cross section presented by each drop.

Once this drop size distribution is calculated, it is useful for quantitative analysis. For example, Rain rate, $R_r$, can recovered from the drop size distribution using

$$R_r = \frac{\pi}{6} \int_0^\infty n(D)D^3 v(D)dD \tag{2.10}$$

This thesis will attempt to use the Marshall-Palmer Z-R relation to validate the DSD estimates. This relation is given as $Z = 200R^{1.6}$, and recovers an approximate reflectivity factor from rain rate. Reflectivity factor values approximated from rain rate should ideally correlate with Z values calculated directly from volume reflectivity.

# CHAPTER 3

# RADAR UPGRADES

Section 3.1 summarizes important aspects of the original hardware configuration. A more detailed description of the original system can be found in [9]. System sensitivity is discuseed in Section 3.2. Section 3.3 encompasses changes made prior to the 2016 deployment. Major changes include the use of a new A/D converter and baseband amplifier to increase sample rate. Section 3.4 includes changes made in between the deployments. Increased receiver gain and a new high power amplifier were the major modifications during this period.

## 3.1 Original Radar Hardware

This section summarizes relevant information on the original hardware of the UMass FMCW radar. The design matches the topology depicted in Figure 2.1.

| | |
|---|---|
| Frequency | 2.94 GHz |
| Bandwidth | 60 MHz |
| Sweep Time | 45 ms |
| Transmit Power | 250 W |
| Range Resolution | 2.5 m |
| Maximum Range | 2.5 km |
| Unambiguous Velocity | $\pm$ 1.1 m/s |

**Table 3.1.** Original UMass FMCW Profiling radar system parameters.

A Sciteq DCP-1378 direct digital chirp synthesizer is used to generate frequency-agile chirps. These chirps are then used to drive the IF port of a single-sideband mixer with a 2.9 GHz source at the Local Oscillator (LO) port. A preamplifier boosts

13

the power, which is divided with a 3 dB splitter into the high power amplifier and to the LO port of the downconversion mixer. An Applied Systems Engineering model 200S Traveling Wave Tube Amplifier (TWTA) with 250 Watt maximum output, and 54 dB of power gain is used for the high power amplifier.

The output of the TWTA is connected to the transmit antenna. Both antennas are identical 8-foot diameter parabolic dish antennas. They feature 34 dB gain at 2.9 GHz and are mounted with one foot of separation on a steel frame. This frame is installed on a pedestal on the bed of an International 4300 for easy transport. Shrouds and radomes protect the antennas from the elements, and RF-absorbing materials along the interior walls of the shrouds improve the isolation characteristics. The isolation between antennas is approximately 98 dB.

The system receiver consists of an LNA with 25 dB gain and 0.9 dB noise figure, a narrow bandpass filter, and a double balanced mixer. The bandpass filter has a center frequency of 2940 MHz, 60 MHz bandwidth, and steep roll-off. The baseband hardware consists of a low-pass filter, op-amp amplifier for audio frequencies (300 Hz - 26 kHz), and an A/D converter with a 46 kHz sample rate. The A/D had accompanying digital signal processing hardware to interface with a Pentium-based host computer [9].

System characteristics before upgrades for VORTEX-SE are summarized in Table 3.1.

## 3.2   Sensitivity

Radar sensitivity is a critical system feature when making clear-air measurements. Dynamic range also becomes important when considering antenna leakage, and stronger signals reflected from rain drops. To see all of the trade-offs, it is useful to construct relations between system and environmental parameters. Since received

power and structure parameter values are related through volume reflectivity, known system parameters can be used to construct a $P - C_{n^2}$ relation, as in Figure 3.1.
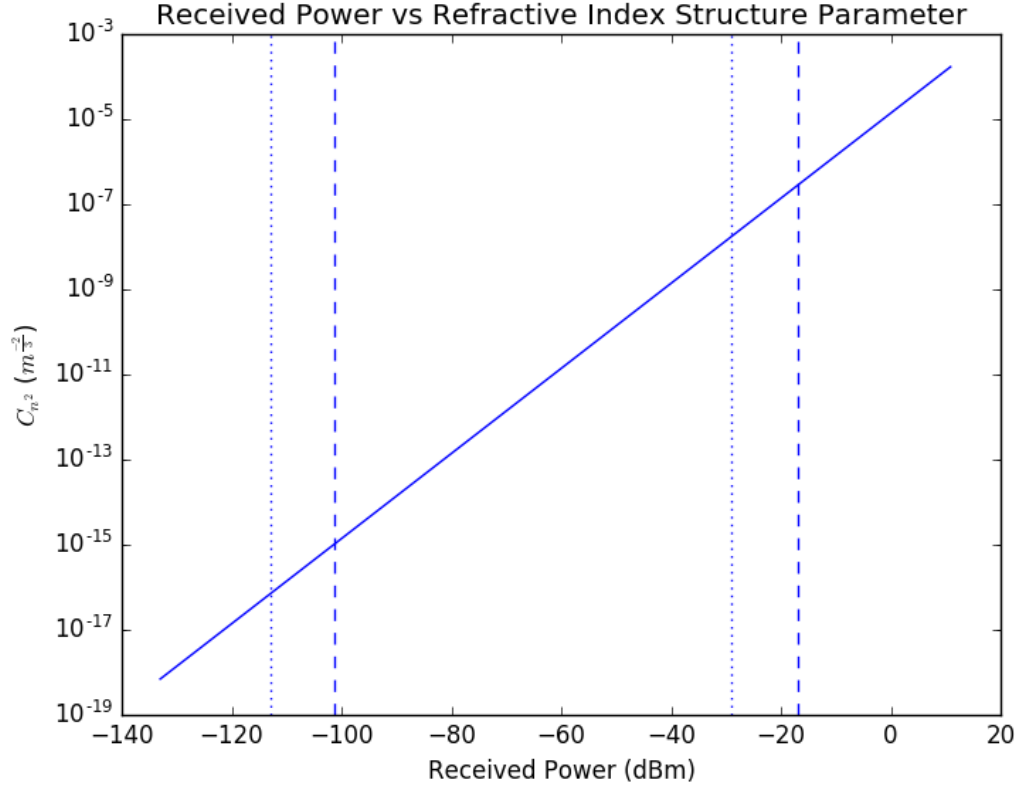


**Figure 3.1.** Relation between received power referenced to the receiver input and refractive index structure parameter.

The vertical axis on this plot represents the structure parameter on a logarithmic scale, and the horizontal represents received power referenced to the receiver input in dBm. A typical structure parameter value obsrerved from scatter from a convective boundary layer could be on the order of $10^{-14}m^{-\frac{2}{3}}$. A linear power to structure parameter relation is observed on this scale. This plot is based on fundamental system parameters such as radar wavelength, transmit power, antenna gain, and range resolution. Since these parameters have not changed significantly in the lifetime of this system, this plot is accurate to a few dB over the instrument lifetime. A similar

plot can be constructed for reflectivity factor, as shown in Figure 3.2. In this figure, the vertical axis is Reflectivity factor in dBZ.

Vertical lines displayed in this received power versus structure parameter plot represent system limits. The dashed lines correspond to system limitations for the 2017 deployment during VORTEX-SE. This shows a minimum detectable signal of approximately -103dBm, and a maximum signal of approximately -20dBm. Theoretical sensitivity performance only changes marginally between 2016 and 2017. Dotted lines represent the original system sensitivity without range correction applied. In the original system, this corresponds to -113dBm minimum detectable signal. This figure is misleading, as the original system sensitivity decreases with range. At a height of 1km, there is approximately 20dB degradation of sensitivity in terms of received power (+20dB shift of dotted lines).

## 3.3   System upgrades, 2016 Deployment

The detailed system block diagram, as configured for the 2016 experiment is shown in Figure 3.3. Figures 3.4 and 3.5 each represent the upconverter and downconverter blocks in Figure 3.3 respectively.

In the system diagram, the components along the top serve to generate the LO signal used to upconvert the frequency chirp to S-Band. CLK1 is a 50 MHz source, which generates the clock signal to lock the phase-locked loop (PLL) of CLK2, the 2.9 GHz source. CLK1 also provides the clock for the DDS, which is an Analog Devices AD9854 evaluation board for VORTEX-SE. The eval board uses this 50 MHz source as a reference for the on-board PLL. The upconverter in Figure 3.4a mixes, filters and amplifies the frequency chirp. The filtering and the single-sideband feature of the mixer ensures the signal is upper sideband. This signal drives the TWTA, which amplifies the signal to 250 W. The antenna feeds were not properly tuned during this deployment, and featured a worst case 7 dB return loss across the band. This implies
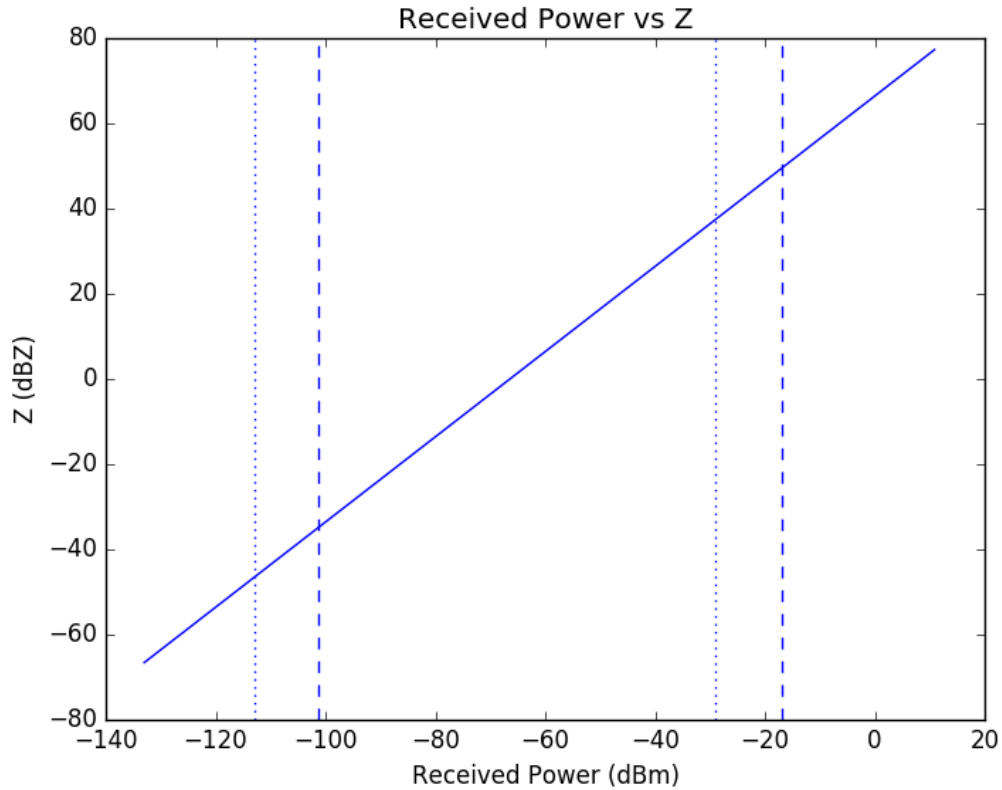
**Figure 3.2.** Relation between received power referenced to the receiver input and reflectivity factor.

several Watts of power are reflected back towards the transmitter, and additional power loss at the receiver input. A circulator is used to direct any reflected power into a load, such that it does not damage the TWTA.

A splitter is used after the preamplifier which couples off a copy of the transmit signal to drive the LO port of the downconversion mixer. The received signal is amplified, filtered and mixed down to baseband by the downconverter in Figure 3.4b. A new low noise amplifier is used to provide increased gain (38 dB) with lower noise figure (less than 0.5 dB). These RF system components and configuration closely match the previous system configuration.

A 30dB coupler is used to couple off a signal at the output of the TWTA. This signal is fed through a surface acoustic wave (SAW) time-delay line into the receiver
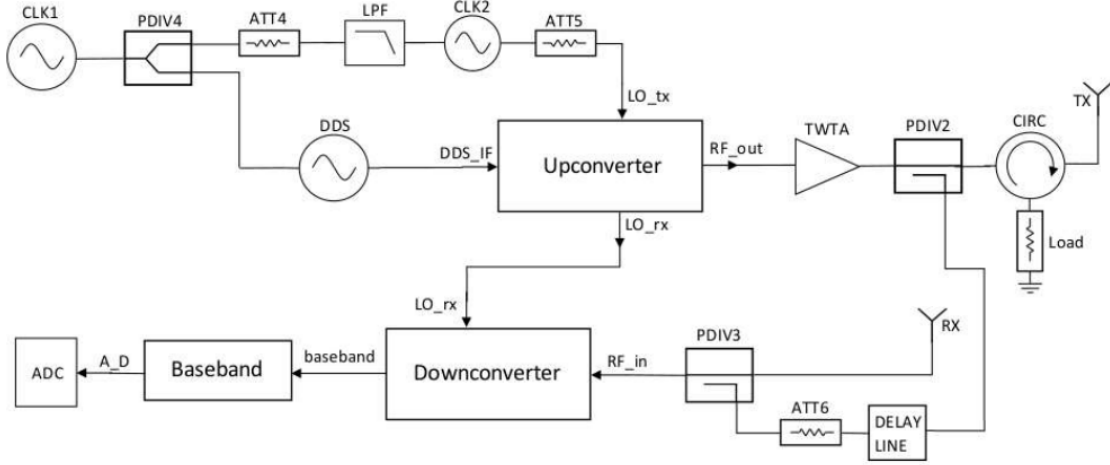
**Figure 3.3.** Radar System block diagram for the 2016 deployment



(a) Up-converter                              (b) Down-converter
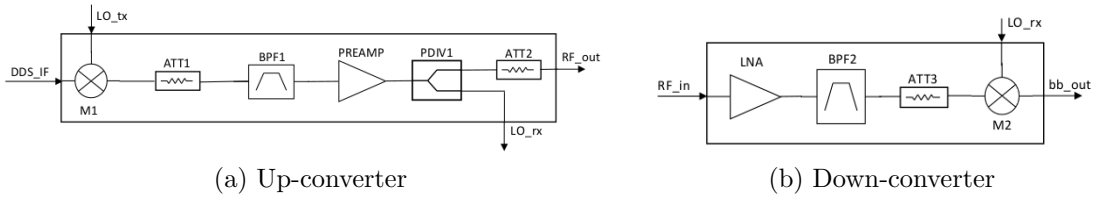
**Figure 3.4.** Block diagram of radar subsystems: upconverter and downconverter

input, to act as a calibration loop. The received signal associated with the delay line signal could be used to correct for fluctuations in system component performance. The delay line was overdriven during this deployment, creating intermittent issues and finally failure of the device by the end of the observation period. The calibration path is thus removed for the 2017 deployment due to cost constraints.
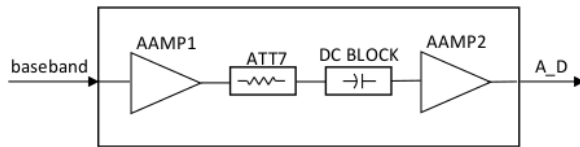


**Figure 3.5.** Baseband subsystem used during the 2016 deployment

Figure 3.5 depicts the baseband hardware, which is new for the 2016 experiment. The amplifiers operate over a wider bandwidth than the previously used op-amps. The DC blocking capacitor acts as a high-pass filter. Since the cutoff of this filter is set towards the top of the baseband frequency range, it serves to reduce the power level of close targets, such as leakage and ground clutter reflections, without affecting the low-level returns from farther targets. The response of this capacitor is roughly approximated as the range-correction needed in the radar range equation. This baseband response is used to mitigate the power level of antenna leakage such that system gain can be increased without saturating the receiver. This improves sensitivity and dynamic range at the higher ranges.

The data acquisition hardware is replaced in conjunction with baseband hardware upgrades. An Ettus USRP N210 Software Defined Radio replaces the old hardware to increase the possible sample rate. The USRP has Digital I/O pins and a D/A converter to set the DDS state and properly synchronize the transmit sweeps with the data acquisition. The physical sample rate of the USRP is 100 MHz, but the integrated FPGA performs digital filtering and decimation to reduce this to an effective sample rate at which data is passed to the host PC. Data collected and referenced to the effective sample rate is sent via Ethernet cable to the host computer for processing. A new Core 2 Duo host computer provides the compatibility and computational power to interface well with the USRP.

The results of baseband hardware modifications include increased maximum sample rate. As discussed in Section 2.1, maximum unambiguous velocity range is limited by radar wavelength and FM-CW sweep time. Increased maximum sample rate allows for faster sweep rates (containing the same number of samples per sweep) which increases the unambiguous velocity range. For the 2016 deployment, the sweep time is decreased by an order of magnitude, leading to significant widening of the unambiguous velocity range.

| Frequency | 2.95 GHz |
|---|---|
| Bandwidth | 30 MHz |
| Sample Rate | 400 kHz |
| Sweep Time | 5 ms |
| Transmit Power | 230 W |
| Range Resolution | 5 m |
| Maximum Range | 5.12 km |
| Unambiguous Velocity | $\pm$ 5 m/s |
| Theoretical Sensitivity | -97 dBm |

**Table 3.2.** FMCW Profiler system parameters for the 2016 deployment.

It is evident from the equations in Section 2.1 that there is a trade-off between system parameters in determining performance characteristics. A faster sweep time increases the maximum unambiguously measurable velocity. Raising the sample rate accordingly compensates to maintain a similar maximum range, at the expense of a corresponding higher data rate. DDS bandwidth and sweep time and the USRP effective sample rate are re-programmable in software, within hardware tolerances. This means radar system characteristics such as maximum range, range resolution, maximum unambiguous velocity and data rate are dynamically adjustable. Other parameters such as velocity and temporal resolutions are easily adjusted in the data processing code. Table 3.2 shows the FM-CW parameters used in the 2016 experiment.

One undesired result of increasing the baseband sample rate is degraded spurious response. The TWTA is powered from switching power supplies clocked at 50kHz. The sideband rejection of these supplies is rated at -50dBc. These sidebands and their harmonics modulate the TWT, and the resultant products fall into the increased baseband sample range. These products degrade data quality during the deployment, and filtering in software is required to mitigate the impact. To minimize the number of products that fall in band, the sample rate was limited for the 2016 deployment.

## 3.4 System upgrades, 2017 Deployment

System configuration for the 2017 deployment is shown in Figure 3.6. The upconverter and downconverter blocks of Figure 3.4 are the same in both the 2016 and 2017 experiments, except for attenuation levels. The receiver attenuation was relatively high during 2016 deployment to prevent non-linear effects and receiver saturation in rain conditions. In 2017, this attenuation was reduced to increase sensitivity, at increased risk of overdriving the USRP.
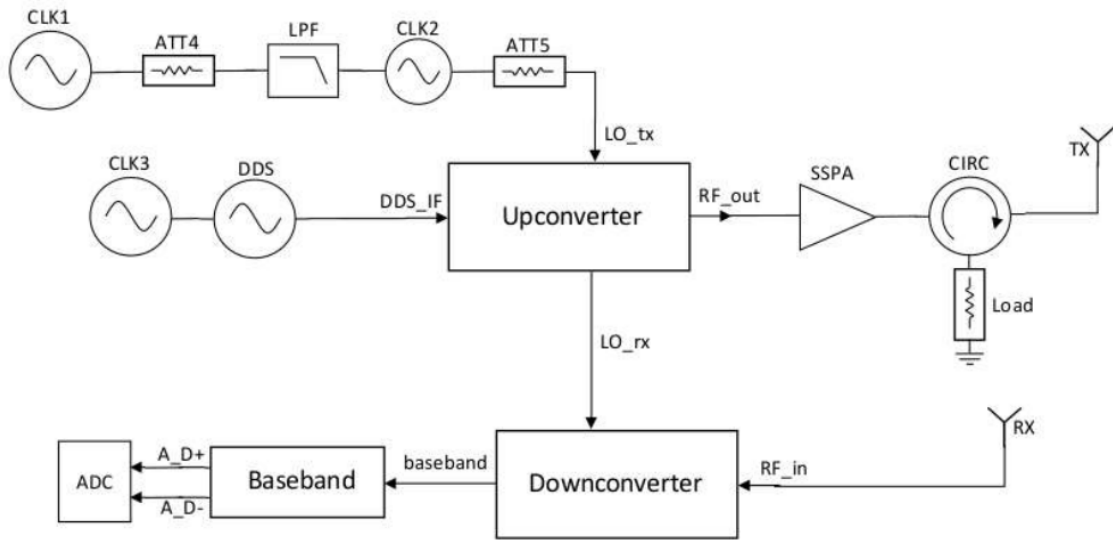


**Figure 3.6.** Radar System block diagram for the 2017 deployment
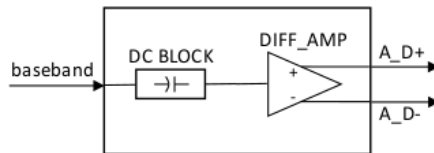


**Figure 3.7.** Baseband subsystem used during the 2017 deployment

Replacement of the TWTA with a Solid-State Power Amplifier (SSPA) (an AM3-3S-54-54R from Microwave Amplifiers Ltd.) drastically improved the system spurious response. The SSPA features a power supply sideband spec of -80 dBc versus the -

50 dBc TWTA spec. This led to a 30 dB improvement in the spec for the most detrimental spurs. Both devices had the same power output, had similar gain, and input power requirements. Both amplifiers had a frequency response that covered the FCC allocated 100 MHz band. The SSPA is also more efficient, generates less heat inside the truck, and operates on 120 volt supply voltage.

Improved spurious response allows several other system changes. Foremost being a simplification of data processing, as two-dimensional median filtering the data is no longer necessary. The poor spurious system response in the 2016 deployment made increased sample rate detrimental, since more of these products would fall in the baseband and interfere with data collection. In 2017, the sample rate is increased by an additional fifty percent. This allows for faster sweep times, and thus increased data rate and higher maximum unambiguously measurable velocity, while maintaining other nominal radar parameters. This higher velocity range is useful for collecting rain data.

| | |
|---|---|
| Frequency | 2.945 GHz |
| Bandwidth | 30 MHz |
| Sample Rate | 588 kHz |
| Sweep Time | 3.33 ms |
| Transmit Power | 250 W |
| Range Resolution | 5 m |
| Maximum Range | 5.12 km |
| Unambiguous Velocity | $\pm$ 7.5 m/s |
| Theoretical Sensitivity | -97 dBm |

**Table 3.3.** FMCW Profiler system parameters for the 2017 deployment.

The second critical change made for the 2017 deployment is the baseband receiver hardware modification. The baseband amplifiers used during the 2016 deployment were replaced with one single ended to differential, balanced op-amp. Using differential signaling here provides high common mode rejection of any signals which may leak into the baseband after the op-amp. Differential signaling is also better suited to

drive the USRP. It requires a differential input voltage centered between its supply voltage and ground. The use of differential signaling maximizes dynamic range. This is due to using the full range of both inputs as opposed to grounding one, as in a single ended topology.

With these sources of interference removed from the system, several low-level system spurs remain. The source of most of these spurs was isolated to interference between the DDS, Ettus and the 50 MHz source, CLK1. By adding a dedicated DDS clock, and introducing additional shielding to the USRP, these spurs were significantly mitigated. The new DDS clock operates at 75 MHz and uses a different PLL multiplication factor. Some spurs are a function of ground clutter and antenna leakage. These can be mitigated somewhat by careful selection of the deployment environment and setting a receiver gain appropriate for the location.

The antenna feeds were also re-tuned for the 2017 deployment. They feature a return loss better than 30 dB across the band of interest. This is a significant improvement over the 7 dB worst case in 2016. In terms of system performance, this corresponds to a radiated power increase of several Watts, less power reflected back towards the transmitter, and less loss at the receiver input.

## 3.5 Software processing

### 3.5.1 Raw Data Processing

The data acquisition code records raw data at the system sample rate. The sample rate is 400kHz during the 2016 deployment and 588kHz during the 2017 deployment. FM-CW parameters are set such that there are a constant number, $I$, of baseband samples which correspond to a single sweep. For VORTEX-SE, parameters were set such that there were $I = 2048$ samples per sweep. The receiver analog to digital converter has 14 resolution bits, leading to 16,384 voltage states. Data processing begins by assembling the consecutive time samples associated with each sweep into

an array, as shown in (3.1), where i represents the index of each sample in the sweep. $J$ sweeps are then stacked up in a two-dimensional array, in this case $J = 256$. Equation (3.2) shows the structure of this array, where $j$ represents the index of a sweep in the series of sweeps, and $v_{j,i}$ represents the voltage sampled at the time corresponding to these indices. ($i$ corresponds to a fine time-scale measurement and $j$ to a course time-scale measurement)

$$v_r(i) = \begin{bmatrix} v_1 & v_2 & \cdots & v_{I-1} & v_I \end{bmatrix} \tag{3.1}$$

Once data is assembled into this array it is multiplied by a two-dimensional Hanning window, and a two-dimensional Fourier transform is applied to the result. The Hanning window serves to mitigate the effect of sidelobes introduced by discontinuities at the edges of the array ($i \approx 0, I$ and $j \approx 0, J$). The Fourier transform converts the fine-scale time domain (i) into the range domain (n), and the course-scale time domain (j) into the Doppler frequency domain (m). The result constitutes a Doppler spectrum, and is an array of the form depicted in (3.3), where $m$ represents the index of each Doppler frequency bin, $n$ represents the index of each range bin, and $V_{m,n}$ represents the complex voltage in each bin. Uncalibrated received power is recovered by taking the element-wise magnitude $S_{m,n} = V_{m,n} \cdot (V_{m,n})^*$. Half of the range bin data in this power spectrum are thrown away. This new Doppler Spectrum consists of 1024x256 elements. The array is then shifted in the Doppler frequency dimension, so as to center the spectrum around the zero Doppler bin. The Doppler frequency domain now corresponds to the velocity domain centered at zero velocity. Finally, several of these spectra are averaged together to form the Doppler Spectrum collected over the given time period. For VORTEX-SE, an averaging number is selected such that the system time resolution is 16 seconds. These spectra are saved as pre-processed datafiles, and other processed data is calculated from these.

$$
v_r(j,i) = \begin{bmatrix} v_{1,1} & v_{1,2} & \cdots & v_{1,I-1} & v_{1,I} \\ v_{2,1} & v_{2,2} & \cdots & v_{2,I-1} & v_{2,I} \\ \vdots & \vdots & \ddots & \vdots & \vdots \\ v_{J-1,1} & v_{J-1,2} & \cdots & v_{J-1,I-1} & v_{J-1,I} \\ v_{J,1} & v_{J,2} & \cdots & v_{J,I-1} & v_{J,I} \end{bmatrix}
\tag{3.2}
$$

$$
V_D(m,n) = \begin{bmatrix} V_{1,1} & V_{1,2} & \cdots & V_{1,N-1} & V_{1,N} \\ V_{2,1} & V_{2,2} & \cdots & V_{2,N-1} & V_{2,N} \\ \vdots & \vdots & \ddots & \vdots & \vdots \\ V_{M-1,1} & V_{M-1,2} & \cdots & V_{M-1,N-1} & V_{M-1,N} \\ V_{M,1} & V_{M,2} & \cdots & V_{M,N-1} & V_{M,N} \end{bmatrix}
\tag{3.3}
$$

### 3.5.2    Software filtering

In each deployment, some spectral filtering is necessary to mitigate the effect of system characteristics in the data, predominantly spurious products during the 2016 deployment and self-interference during the 2017 deployment. Examples of these system characteristics are illustrated in detail in Chapter 4. A median filter is applied to the Doppler Spectrum in order to smooth out discontinuities within a neighborhood. For processing of 2016 data, system spurious products were detrimental to data analysis. These products would drift in range and velocity within a neighborhood of several bins over one system sample period. A two-dimensional median filter of 15 bin width and height was applied to this data, as it seemed to mitigate these products without compromising other data significantly. During the 2017 deployment, there was a system feature which manifested as streaks across range at constant velocity in the the period of one averaged measurement. The worst of this interference was mitigated by applying a 7 bin median filter across the Doppler frequency dimension.

### 3.5.3 Post-Collection Processing

The first parameter calculated from the Doppler spectrum is the estimated noise floor value. This noise floor versus range is assumed to be the median value across the velocity axis in each averaged Doppler time frame. This assumption is made in order to compensate for fluctuations in the measured noise floor over long periods of time. The noise estimate will be biased high in the case of data which spans the majority of the velocity axis. For example, rain data consists of a distribution of rain drops which fall at different velocities; if this data occurs in a significant portion of the velocity bins at any range, it will bias the median value higher for that range bin. To correct for artificially high noise estimates, median values are compared to a noise floor measured for the system with the receiver input terminated. If the median value exceeds this measurement within a certain threshold, it is reset to this terminated input measurement. When enough noise estimate bins in a single spectrum exceed the threshold, the noise estimate will be reset at every range.

Signal to noise ratio is found by calculating the zeroth moment of the Doppler Spectrum for each time bin, as in (3.4). Dividing the resulting power by the noise floor estimate yields the SNR. By using the theoretical noise floor value, this SNR can be calibrated to the received power. Using theoretical and measured radar system constants, volume reflectivity can be solved via Equation (2.4). From volume reflectivity, the refractive index structure parameter and reflectivity factor can be calculated in relevant environmental conditions.

$$SNR(n) = \sum_{m=0}^{M} S_f(n,m)\delta f \tag{3.4}$$

Velocity data is typically found as a function of range and time from the first moment of the Doppler Spectrum, as $M_1 = \sum_{m=0}^{M} f * S_f(n,m)\delta f$

Due to the linear weighting intrinsic in this calculation, this equation will have errors in cases where there are multiple or distributed targets which alias in velocity.

Take as an example a system with unambiguous velocity range of $\pm 5 \frac{m}{s}$ with two targets of equal radar cross section and $-3\frac{m}{s}$ and $-6\frac{m}{s}$ velocities. The system effectively measures the faster moving target as having a $+4\frac{m}{s}$ velocity due to aliasing effects. The previously discussed first moment equation would calculate the mean Doppler velocity as $+0.5\frac{m}{s}$.

To mitigate the effect of aliased data biasing the mean Doppler velocity measurement, the first moment is weighted by angular frequency instead of linear frequency, as governed by (3.5). Velocity is then found by taking the angle of this new first moment and using the typical Doppler frequency to velocity relation as discussed in Section 2.1. Using this calculation for the above example yields the desired mean Doppler velocity of $-4.5\frac{m}{s}$.

$$M_1(n) = \sum_{m=0}^{M} S_\omega(n,m) * e^{j\omega} \delta\omega \tag{3.5}$$

# CHAPTER 4

# SYSTEM PERFORMANCE AND COLLECTED DATA

During the experiment, fifteen weeks worth of data were collected. In analyzing the data, it is important to separate system characteristics from environmental returns of interest. This section starts by detailing the system characteristics evident in the dataset collected during the 2016 deployment. These characteristics are discussed first as they appear in the Doppler Spectrum, and then examined in other parameters. Then, system characteristics from the 2017 dataset are discussed in a similar manner. Finally, several non-environmental features evident in the VORTEX-SE dataset are summarized.

## 4.1 System Characteristics, 2016 Deployment

As discussed in Chapter 3, the spurious system response during the 2016 deployment was problematic. The full group of spurious products is best viewed in the Doppler Spectrum. Several spurs show up at zero Doppler, such as ground clutter and antenna leakage. These products are easily removed, since data of interest does not typically occur at zero velocity. The most problematic spurs have a non-zero Doppler frequency, and shift around within a neighborhood over several time bins.

Figure 4.1 shows a snapshot of the uncalibrated, unfiltered Doppler Spectrum from the 2016 deployment. This data was selected from March 29th 2016 at 8:00-UTC, due to few environmental data features appearing. The spectrum depicted is the result of the two-dimensional Fourier Transform and averaging over sixteen seconds of collected data. The vertical axis is in terms of range in meters from zero to 5km,
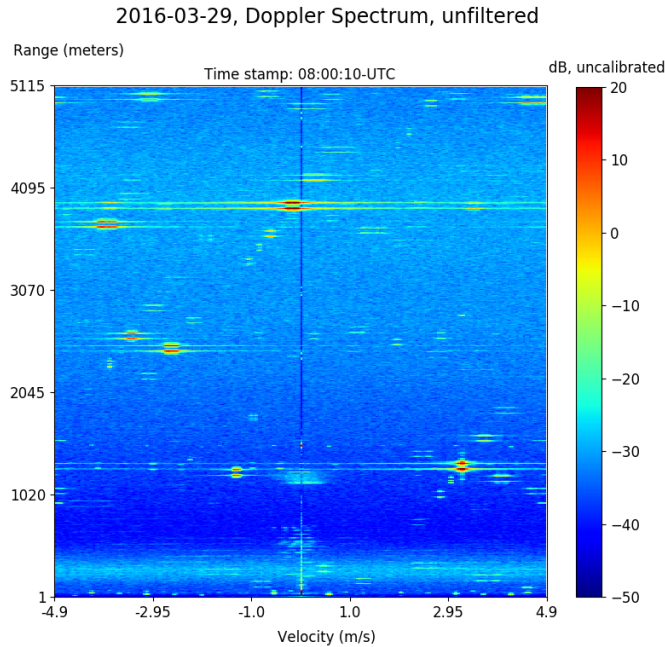
**Figure 4.1.** Sample uncalibrated Doppler spectrum, illustrating spurious response for the 2016 deployment

and the horizontal axis is referenced to velocity and spans from $-4.9\frac{m}{s}$ on the left to $+4.9\frac{m}{s}$ on the right. This data is not calibrated. Intensity of each bin corresponds to the relative received power in that bin, in dB. The following paragraphs detail sources and behavior of these products.

The brightest products, appearing as two dots spread across several bins of the velocity axis at approximately 1250, 2500, and 3750 meters, are caused by the TWTA. The amplifier's internal switched power supplies have a 50 kHz clock rate and 50 dBc sideband specification. These sideband products modulate the transmit signal, creating frequency-shifted and attenuated copies. Each sideband product appears similar to how a point target would in the raw data. Since the products have a relatively high power level, they mix with the antenna leakage and other signals to create additional lower-level products. These sidebands tend to shift within a neighborhood in Doppler frequency over the time, even within one sixteen second

29
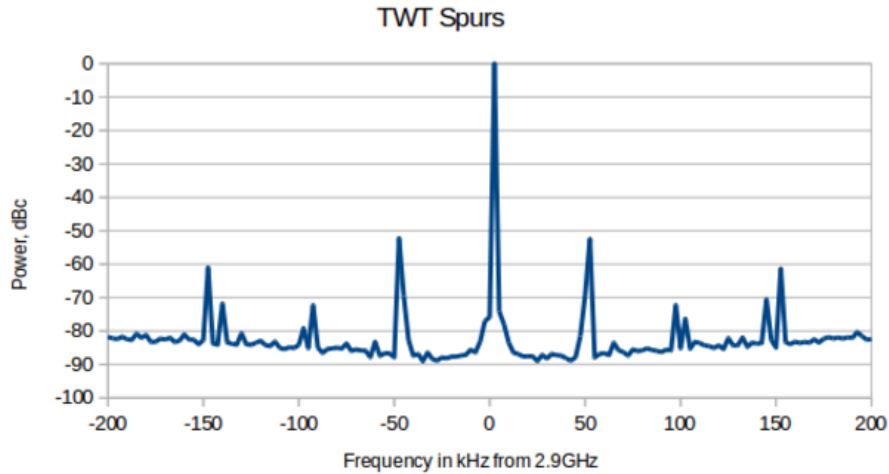
**Figure 4.2.** Measured TWTA output power spectrum with a 2.9 GHz input tone.

sample period. This creates the broad velocity characteristic seen in the Doppler Spectrum plot. The apparent range of these products is stationary, since the switching frequency remains constant on this time scale, or within a given FM-CW sweep. Unfortunately, the first harmonic occurs at just over 1 km, which often contains data of interest.

Figure 4.2 shows the spectral output of the TWTA with a 2.9GHz tone at the input. The vertical axis represents power level relative to the desired output tone. The horizontal axis is frequency deviation in kHz from the 2.9 GHz tone. The first three sideband products are evident above -80dBc, and within 200kHz of the carrier. These sidebands are present on the carrier signal, which is the FM-CW sweep. When returns from these sideband products are received, either as returns from scatterers or in direct antenna leakage, they appear as additional targets sifted in range and velocity. In this case, the 50 kHz sideband appears as a target at a height of 1.25km. The third-order product appears at 150 kHz, or an apparent range of 3.75 km. The equivalent velocity characteristics of these products drifts slowly in the course of a

day, but can also change instantaneously when the compressor in the vehicle's roof-mounted air conditioner turns on.

Another system characteristics evident in Figure 4.1 is the band of noise which spans the velocity axis of the Doppler Spectrum between approximate ranges 100 and 400 meters. This band of noise is also associated with the TWTA. When the amplifier is enabled, it creates this interference in the receiver. This interference occurs even if the receiver input and amplifier output are terminated in with 50 Ohm loads, and is mitigated as distance between the TWT and receiver increases. Implementation of the Differential Baseband receiver hardware removed this interference, and no similar interference is evident after integration of the SSPA.

There are several remaining low power spurious products which exhibit different behavior in Figure 4.1. For example, the product seen at a range of 700 meters and 2.75 $\frac{m}{s}$ is associated with the receiver. A harmonic of this signal is evident at 1.5 km. These products tend to appear consistently in range and move quickly across the velocity axis between sixteen second sample periods. These products are associated with the interaction between the DDS and USRP. By providing the DDS a dedicated clock and further shielding the USRP, these products were mitigated.

In Figure 4.1, the signal at approximately 1250 meters and between $\pm 1 \frac{m}{s}$ an environment signal. The small echo at around 500 meters at low velocities are also environmental. These will be discussed in detail in Chapter 5.

All 2016 data was collected using the same system configuration, and these spurious products are present throughout the dataset. A median filter was applied to the Doppler spectrum to mitigate the effect of these products on data. Figure 4.3 shows a comparison of the same spectrum discussed above before and after the 15 by 15 median filter is applied. In this figure, data below -30 dB/bin is set to black for convenience. Several products were removed, and the most severe were mitigated. The spurious products occurring just above 1 km are at heights which typically interfere

31

(a) Unfiltered image          (b) Filtered image
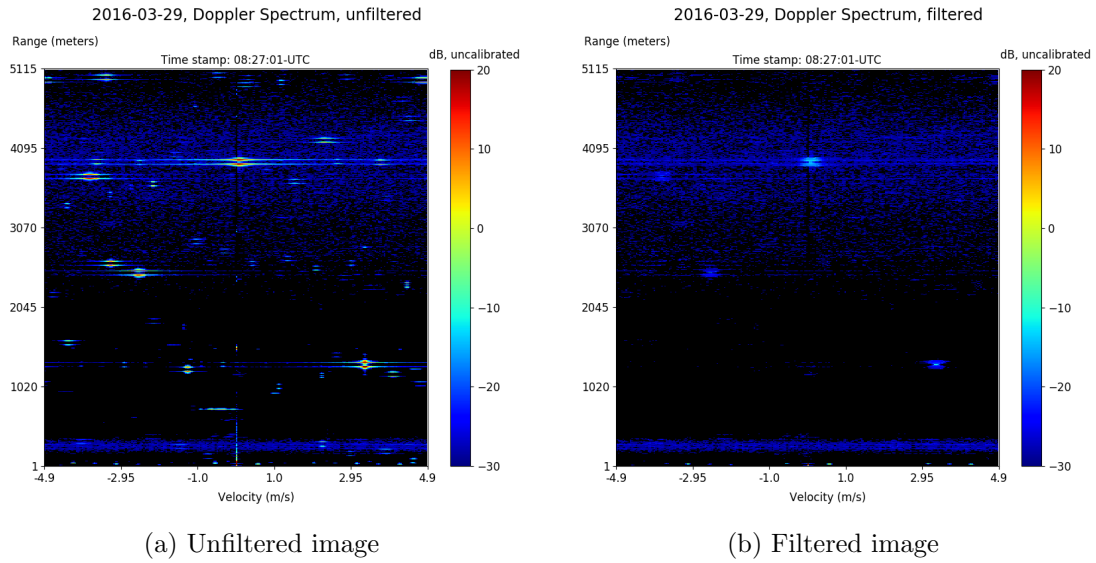
**Figure 4.3.** Sample comparison of the uncalibrated Doppler spectrum illustrating spurious response for the 2016 deployment, unfiltered vs filtered

with environmental clear-air data. The noise band of tube amplifier interference is largely unaffected by the median filtering.

This filtered Doppler Spectrum is used to calculate other parameters including the estimated noise floor, signal to noise ratio (SNR) and velocity. Figure 4.4 shows the noise floor estimate constructed for the hour starting at 8-UTC on March 29, 2016. This data is constructed from median values from each bin of the instantaneous Doppler spectra from each 16 second sample interval, summed over the velocity axis. This is compared to the same value measured with terminated receiver input. Data which exceeds a threshold above this value is reset to this terminated input measured value. Reseting noise estimates in this way is done to prevent various data features from biasing the noise floor and biasing the calibration. The vertical axis on this plot shows range in meters, while the horizontal axis shows the time in minutes.

Several horizontal lines of lower noise power are evident spanning the time domain at constant range in this noise estimate plot. These occur at ranges where system

32

spurious products appear as the median. These values exceeded the noise threshold, and were reset to the terminated receiver input measurement.

Data in the first 200 range bins of the noise estimate plot were also replaced with the terminated input measurement during the 2016 deployment. This is because the TWTA noise band appears in the median value. By replacing these values, the amplifier noise appears in the data as a signal instead of as noise, which maintains the calibration for environmental signals.
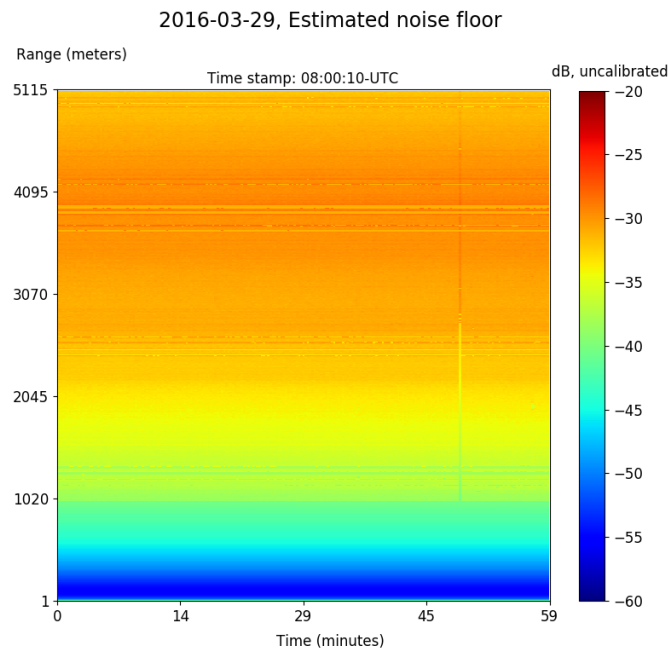


**Figure 4.4.** Sample noise floor estimate, illustrating spurious response for the 2016 deployment

Figure 4.5 shows the SNR measured during the same time period as discussed above. The signal to noise ratio is constructed by taking a sum over the velocity dimension of the time-averaged Doppler spectra in each range and time bin. This plot spans 5km on the vertical axis, and one hour on the horizontal. The TWTA spurs are evident as horizontal lines with ranges corresponding to where they appear in the Doppler spectrum. The band of increasing SNR in the lowest few hundred meters of

the plot is the signal corresponding to TWTA interference noise. The discontinuity evident in the range dimension at 1 km is an effect of replacing the early 200 noise estimate bins with the terminated input measured value. The estimated noise floor fluctuates slowly over the course of a day, causing this discontinuity to fluctuate as well. SNR values lower than -10 dB are set to black to make the figure easier to view.
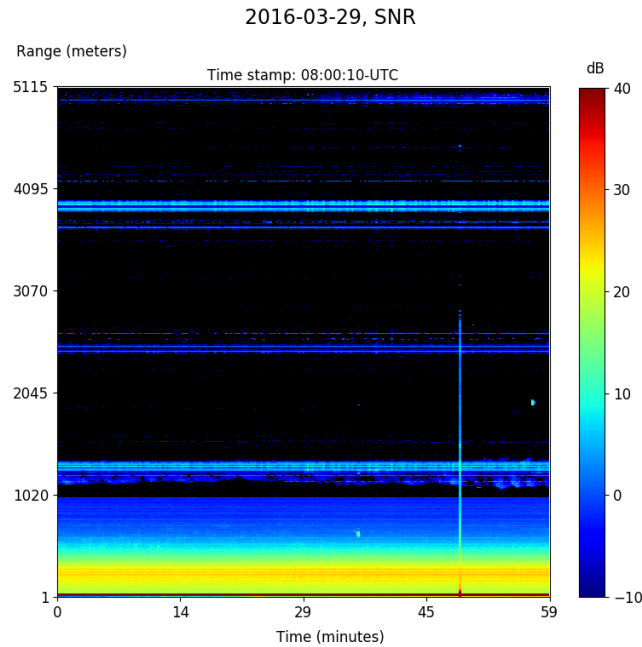


**Figure 4.5.** Sample signal to noise ratio, illustrating spurious response for the 2016 deployment

Velocity measured during the same time period as data discussed above is pictured in Figure 4.6. The TWTA spurs are evident as horizontal lines corresponding to those in the noise and SNR plots. It it interesting to note that their apparent velocity fluctuates over time. In this plot, velocity color is set to black where the SNR is less than -10 dB. This eliminates the random velocity associated with noise. In the lowest 1 km, random velocity measurements are not removed because the TWT interference band biases the SNR higher than -10dB. Non-random velocities in this range correspond to the velocity of actual signals.
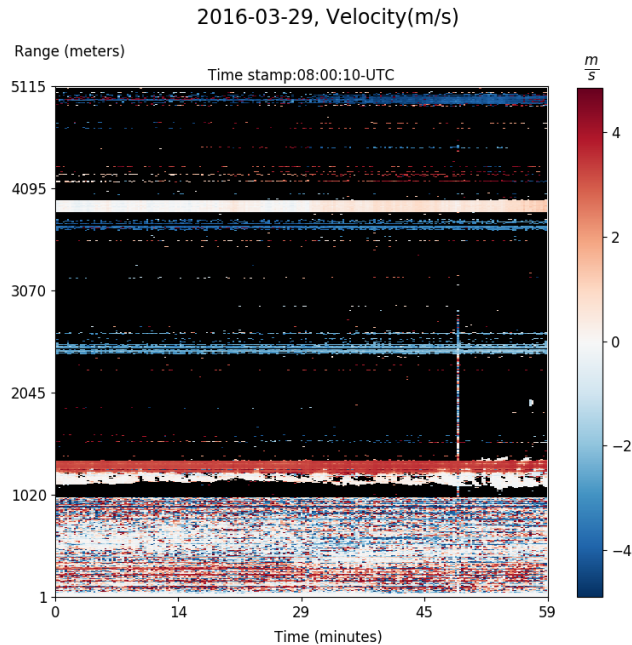
**Figure 4.6.** Sample velocity, illustrating spurious response for the 2016 deployment

## 4.2 System Characteristics, 2017 Deployment

An example of 2017 system performance is presented using data collected on April 9th, 2017. Figure 4.7 shows the Doppler Spectrum collected at 8:41-UTC. This data was selected as having relatively little environmental data. Environmental signals appear more clearly in data collected during 2017 as the system sensitivity is higher. Some of these data features are from environmental scattering, and others from the system. This Doppler Spectrum is the result of averaging the instantaneous Doppler Spectrum over 16 seconds. The vertical axis on the plot spans 5 km in range. Since unambiguous velocity range was expanded for 2017, the horizontal axis spans $\pm 7\frac{m}{s}$. Data below -30 dB is displayed as black for convenience.

There is a set of spurs and two harmonics evident in the system during the 2017 campaign. These spurs are very close to the noise floor, and are not as destructive to viewing the data as spurious products were during the 2016 deployment. The products behave similarly to the TWTA spurs, occurring at constant range and varying in

35

velocity. The third harmonic is seen in Figure 4.7 at a range of 3.5 km and -5$\frac{m}{s}$. The second and first harmonic appear at ranges 2.3 km and 1.2 km, respectively. These spurs are a system product, but beyond this the cause is unknown.

The more interesting system features manifest as streaks across the range dimension. These are evident in Figure 4.7 at velocities of $\pm 1.5\frac{m}{s}$. These streaks are a system characteristic, and tend to shift in velocity over time. This interference is evident throughout the 2017 experiment. It is likely a function of the system rather than the environment, as changes in location do not seem to mitigate the effect. The specific cause is unknown. This feature does not interfere significantly with clear-air environmental data.
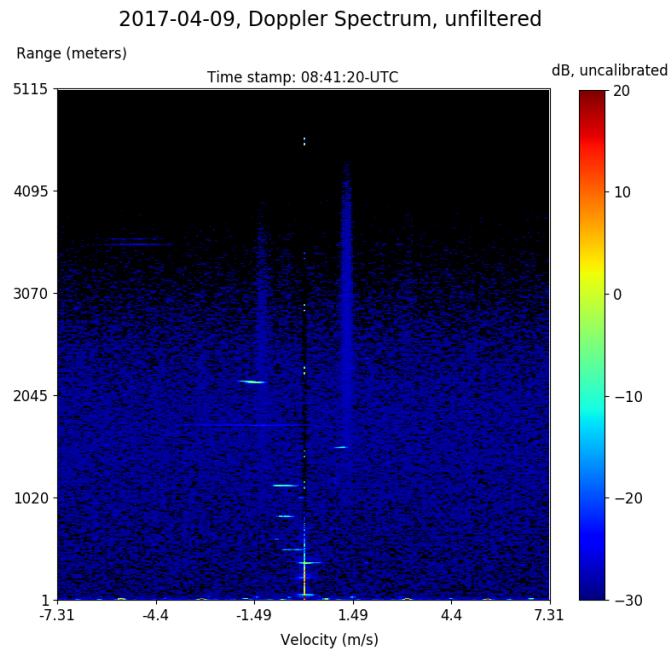


**Figure 4.7.** Sample Doppler Spectrum, illustrating system performance for the 2017 deployment

This effect in the data is slightly mitigated by applying a horizontal median filter of a 7 bin width. Remaining plots presented in this section are from data collected on March 30th, 2017. Figure 4.8 shows the Doppler spectrum before and after the median

filter is applied, with data collected at 8:06-UTC. In this case, the self-interference occurs at a velocity of $\pm 7\frac{m}{s}$. There are also much weaker copies on either side of the line. The highest intensity line is mitigated in the filtered version. The remaining lines are unaffected, as they are very close to the noise floor.



(a) Unfiltered image        (b) Filtered image
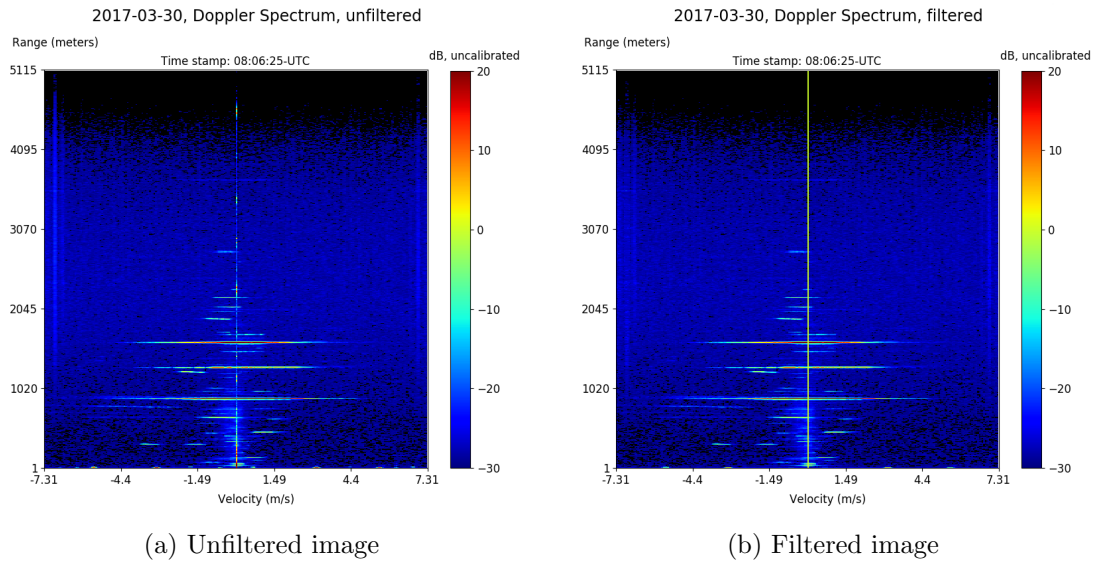
**Figure 4.8.** Sample Doppler Spectra, illustrating median filtering for the 2017 deployment

The interference described above carries through to other parameters, but is so close to the noise floor, that it does not typically disrupt the data. Figure 4.9 shows a full hour of collected SNR returns from March 30th at 8-UTC. The horizontal lines visible at 3.5 km and 1.2 km are a result of the system spurs. The solid vertical lines visible at 25, 35, and 38 minutes are examples of receiver saturation. Other data features in this plot are environmental.

Figure 4.10 shows the estimated noise floor over the same time span on March 30th. The vertical axis represents range, and the horizontal axis represents time in minutes. This plot spans 5 km and 1 hour. In this plot, there are a few vertical lines of lower power. These are a result of receiver saturation, which causes the noise floor to exceed the noise threshold and be reset to the terminated input measured value.
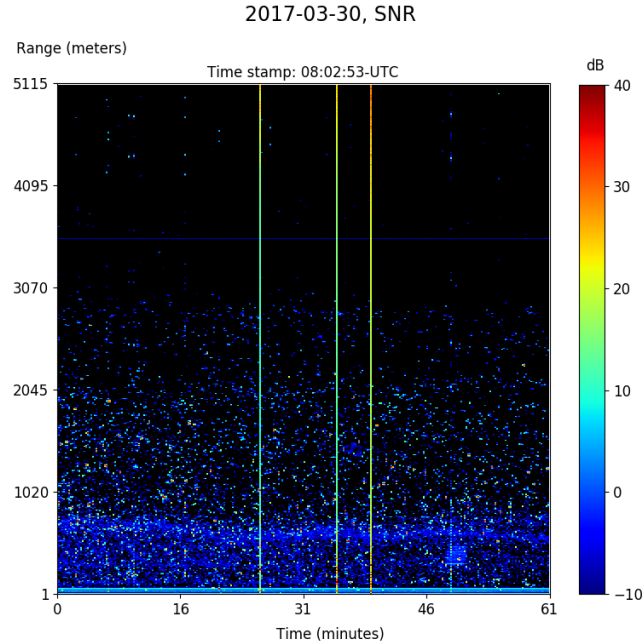
**Figure 4.9.** Sample SNR, illustrating system performance for the 2017 deployment

Figure 4.11 shows the velocity measurement over the same time span on March 30th. In this plot, the vertical axis represents range and the horizontal represents time. Compared to the data collected in 2016 this data features an increased velocity range, corresponding to a different intensity to color mapping. The horizontal lines are a function of the spurious products. The vertical lines are artifacts of receiver saturation. Other data features are environmental.

On April 6th 2017, the radar experienced relatively destructive interference from the vertical lines of higher intensity which appear in the Doppler spectrum. In an attempt to mitigate the effect, the frequency of the FM-CW sweep was shifted. The result was mitigated interference, with the added result of dropping the noise floor estimate. This is likely a product of the noise floor estimate being biased higher by this interference before this adjustment in the sweep frequency mitigated the effect. The sweep frequencies were adjusted once at 23:56:31-UTC on April 6th, and a second time at 00:35:33-UTC on April 7th.

38
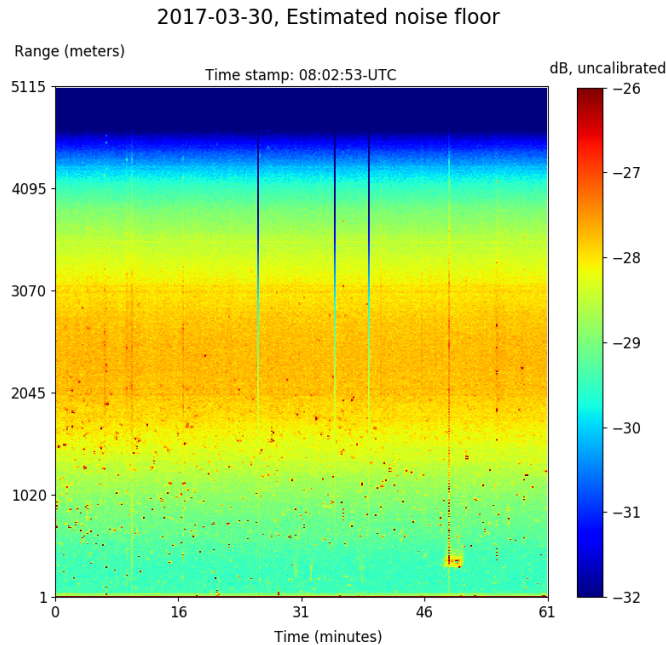
**Figure 4.10.** Sample noise floor, illustrating system performance for the 2017 deployment

Figure 4.12a shows the noise floor estimate during the hour where the first sweep adjustment occurred. The drop in noise floor is evident as the discontinuity in time of noise floor in the last few minutes of the plot. Figure 4.12b shows the hour during which the second sweep adjustment occurred. The noise floor drop in this plot is evident as the sharp discontinuity just after the thirty minute point. In total, the noise floor is approximately 3 dB lower at higher ranges, and approximately the same at low ranges after that day.

The source of changes in this noise floor estimate is best viewed in the Doppler spectrum. Figure 4.13 shows the unfiltered Doppler Spectrum for the sweeps immediately before and after the sweep adjustment. The vertical streaks abruptly shift in velocity, and decrease in magnitude between these sweeps. Rapid, discontinuous changes like this are not typical characteristics of these products. A similar change occurs during the second sweep frequency adjustment, seen in Figure 4.14

39
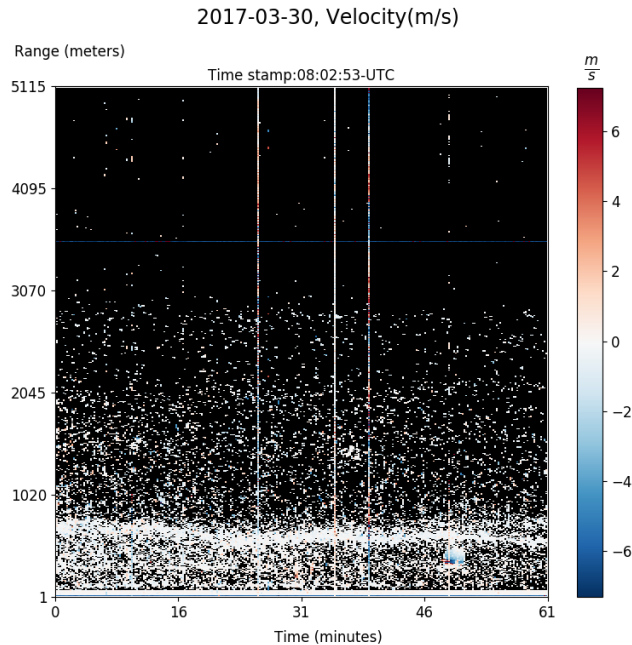
**Figure 4.11.** Sample velocity, illustrating system performance for the 2017 deployment

## 4.3 Non-Environmental Features Evident in Dataset

Several other non-environmental effects occur in the data throughout the course of the experiment. Some examples are discussed below.

There are errors in estimating the noise floor when high level signals are present. Figure 4.15 shows the noise floor and SNR when the magnitude of several system spurs exceeds the threshold and is reset to a measured value. These areas of lower noise floor estimate correspond to a higher value of SNR. In this case the SNR plot may appear to show a target, or at least a change in the system spurious response. This change is only due to the noise floor estimation.

On April 2nd 2016, at approximately 22:20-UTC, there was an apparent drop in the floor of SNR. The cause of this is unknown, but data collected before this point observes the higher SNR floor value, and data after shows the lower value. Figure 4.16 shows the change in the minimum SNR values evident after 22:20-UTC. The
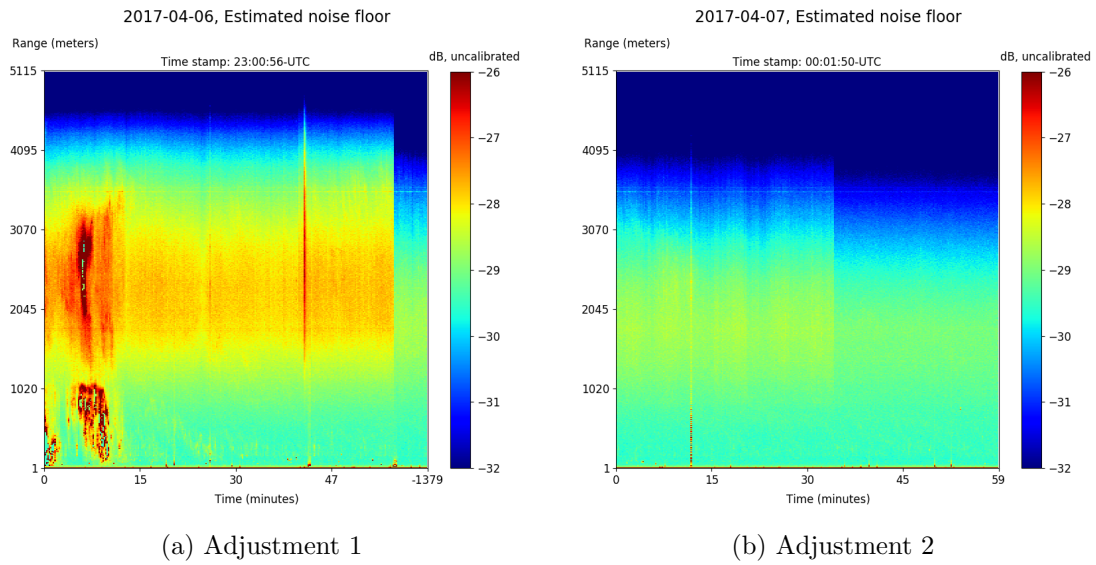
**Figure 4.12.** Noise floor estimate plots illustrating interference changes corresponding to sweep frequency adjustments during the 2017 deployment

effect on the data of this change is negligible. Oddly, the noise floor estimate was unaffected by this change.

During the 2016 deployment, there was a degradation of system spurious response for unknown reasons. Starting on April 29th at 3:30-UTC, the system response shifted and significantly more products appeared. Figure 4.17 shows the difference in number of spurious products before and after this degraded system response. The Doppler Spectrum suggests that a few bright targets appeared at approximately 1km and 1.75km, mixing with TWT sidebands and antenna leakage to create additional spurious products. Figure 4.18 shows the SNR during the hour in which the response changed.

(a) Before adjustment

(b) After adjustment
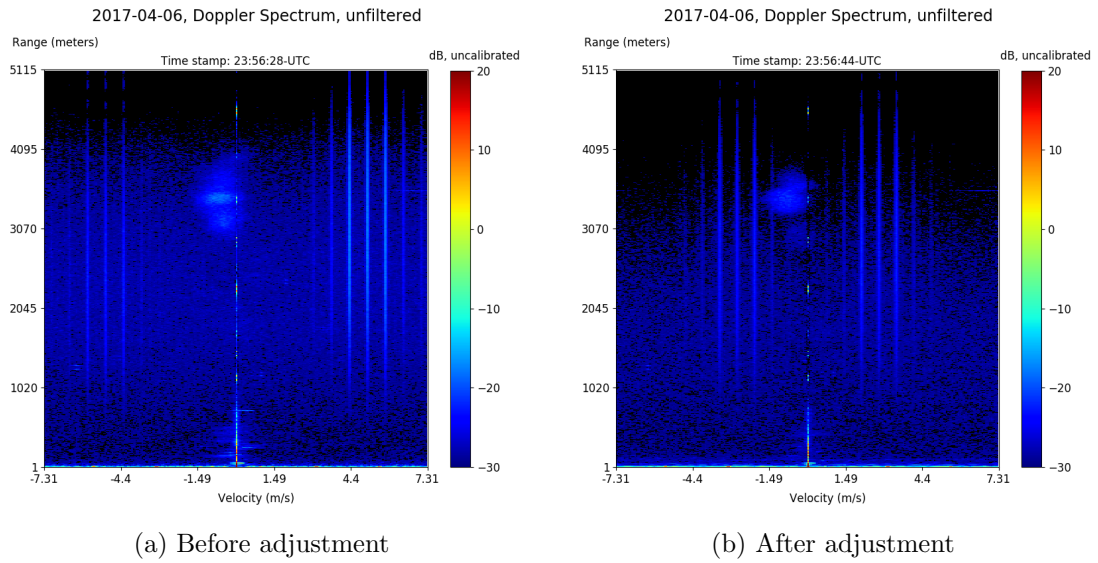
**Figure 4.13.** Doppler Spectrum, comparison of interference due to first FM-CW sweep frequency adjustment



(a) Before adjustment

(b) After adjustment
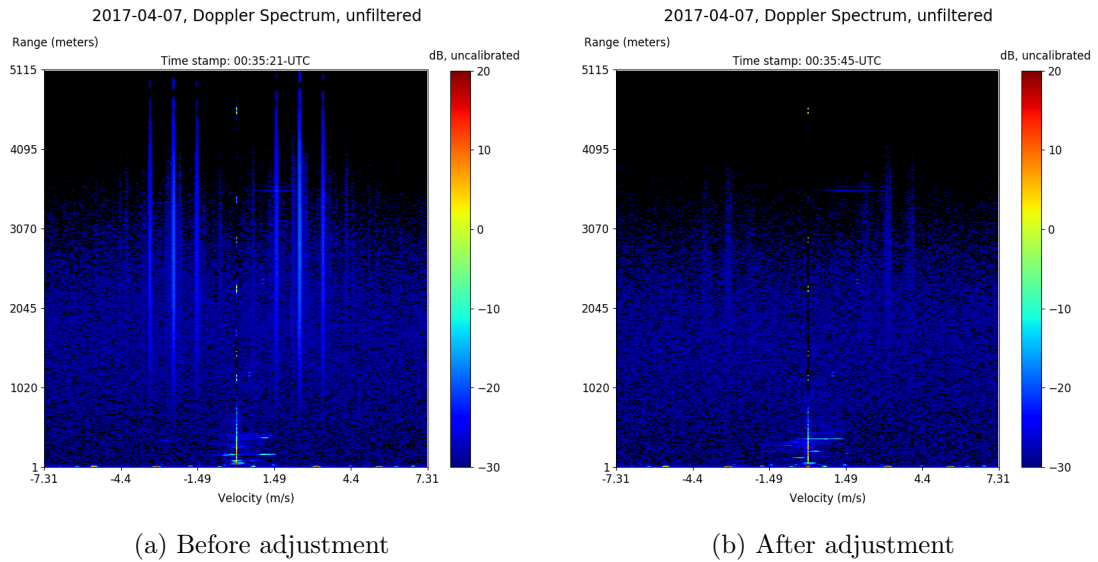
**Figure 4.14.** Doppler Spectrum, comparison of interference due to second FM-CW sweep frequency adjustment

(a) SNR

(b) Noise floor estimate
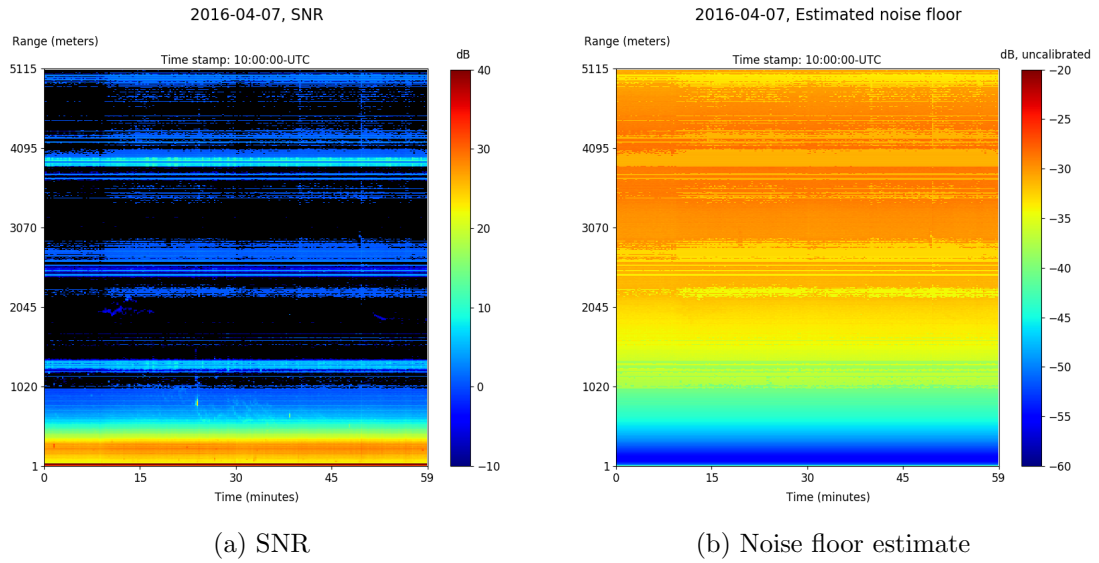
**Figure 4.15.** Example of a noise floor estimation error, due to high spur magnitude.
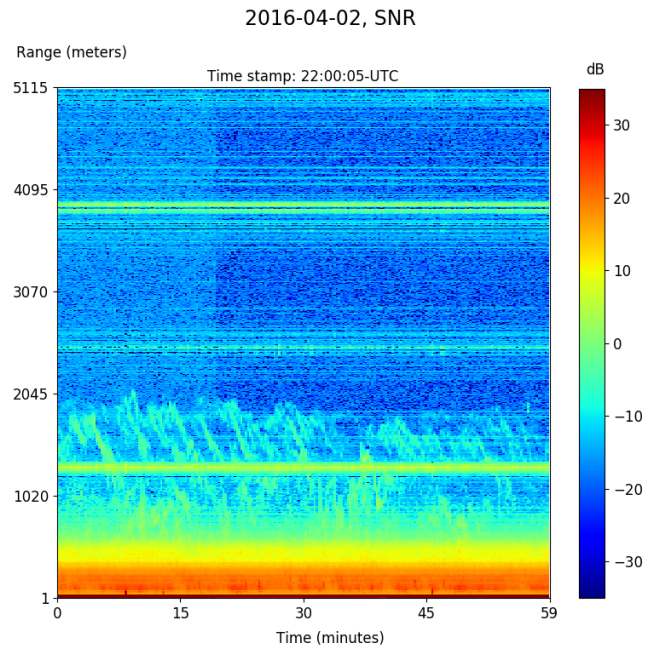


**Figure 4.16.** Plot showing the drop in SNR minimum during the 2016 deployment.

(a) Before degredation
(b) After degredation
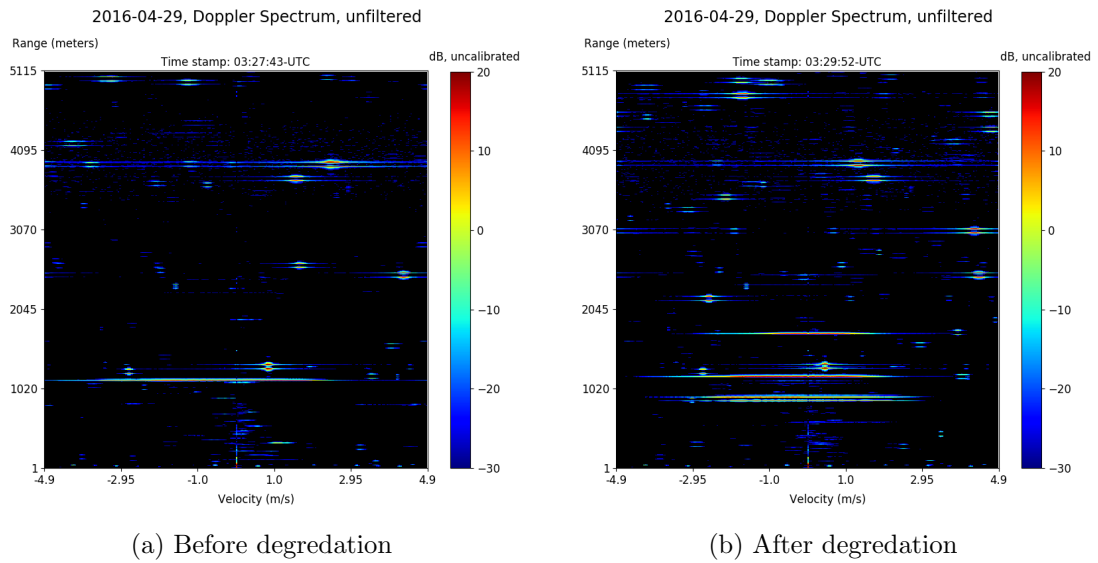
**Figure 4.17.** Doppler Spectra illustrating degradation of spurious response occurring on April 29th, 2016.
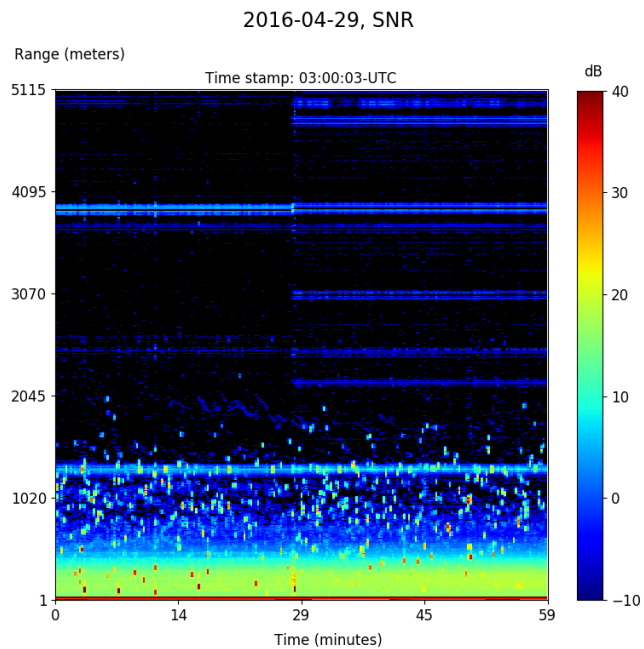


**Figure 4.18.** SNR plot illustrating degradation of spurious response occurring on April 29th, 2016.

# CHAPTER 5

# CLEAR AIR DATA

Historically, this instrument was used as a vertical wind profiling radar to analyze clear-air returns. This included reflectivity information, the refractive index structure parameter was calculated from this. Increased system velocity range also gives this instrument ability to fully characterize vertical wind speeds in the ABL. This chapter illustrates typical environmental data features collected under clear-air conditions. Data from 2017 is used since thre is less system interference. All time is referenced to the UTC timezone. Data was collected in the CST time-zone, which is UTC-5 hours.

## 5.1    The Atmospheric Boundary Layer

The ABL transitions between states over time, and each state looks different in the data. In this section, examples of a stable boundary layer and several convective boundary layers are discussed.

A residual boundary layer is a stable state with little energy, where the boundary is relatively constant with height. Figure 5.1 shows the SNR and velocity of a residual boundary layer. The figure starts just after local sundown on April 29th, 2017, and spans from 0 to 7 UTC on the horizontal scale. The vertical scale spans 5 km. This residual boundary layer is evident decreasing from approximately 2 kilometers at 0-UTC. Velocity is depicted in Figure 5.1b. Both the SNR and velocity plots span 5 km on the vertical scale. Data is set to black where the SNR is less than -10 dB, such that the velocity of small signals are not visible. In this plot, no significant convection is evident below the boundary layer.
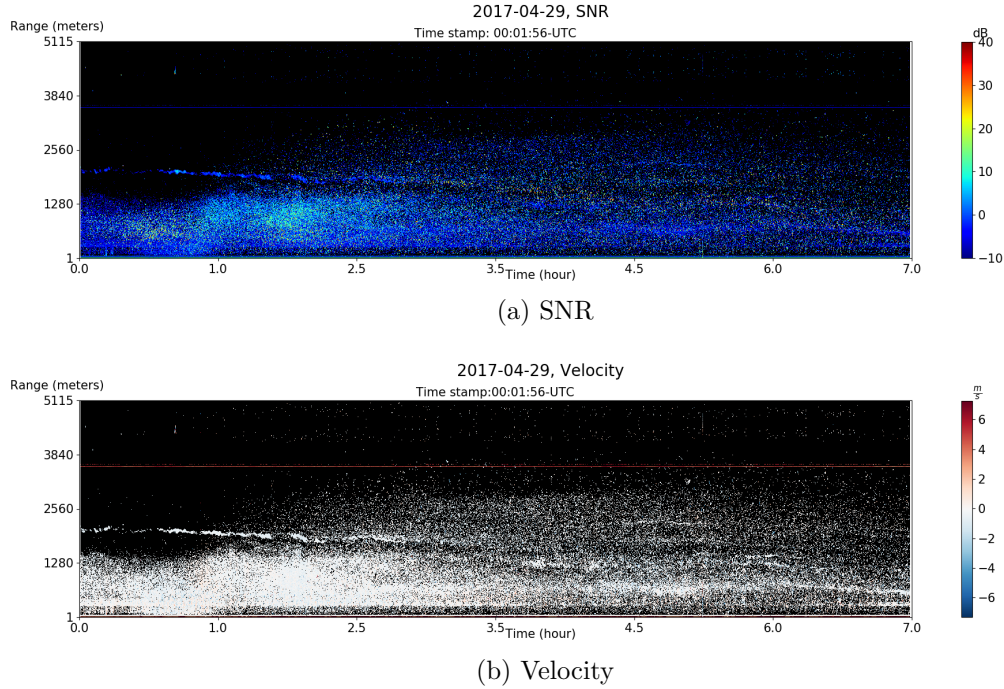
**Figure 5.1.** SNR and Velocity plots for the residual boundary layer from April 29th, 2017. Data displayed from 0 to 7-UTC.

A convective ABL is a more energetic state. Convection occurs when energy from the sun radiates and is absorbed by the surface of the Earth. Air parcels near the surface become hotter than that of air above them, and rise. These air parcels stop rising at the top of the ABL. A typical convective boundary layer example is pictured in Figure 5.2. This data was collected on April 29th, 2017 from 12 to 24-UTC. This corresponds to 7 to 18-CST, in other words local sunrise occurs towards the start of the plot and sunset occurs towards the end. SNR plots are useful for identifying development of boundary layer over time. The boundary layer builds up in height in the morning, until it reaches equilibrium. It roughly maintains its height throughout the afternoon, and starts to drop off in the evening as the sun sets and the convective energy dissipates. The top of the boundary layer appears as a relatively bright line, starting at approximately 600 meters and rising to 1300 meters at its peak.

46

Alternately rising and falling parcels of air in the velocity plot are a characteristic of a convective state.



(a) SNR
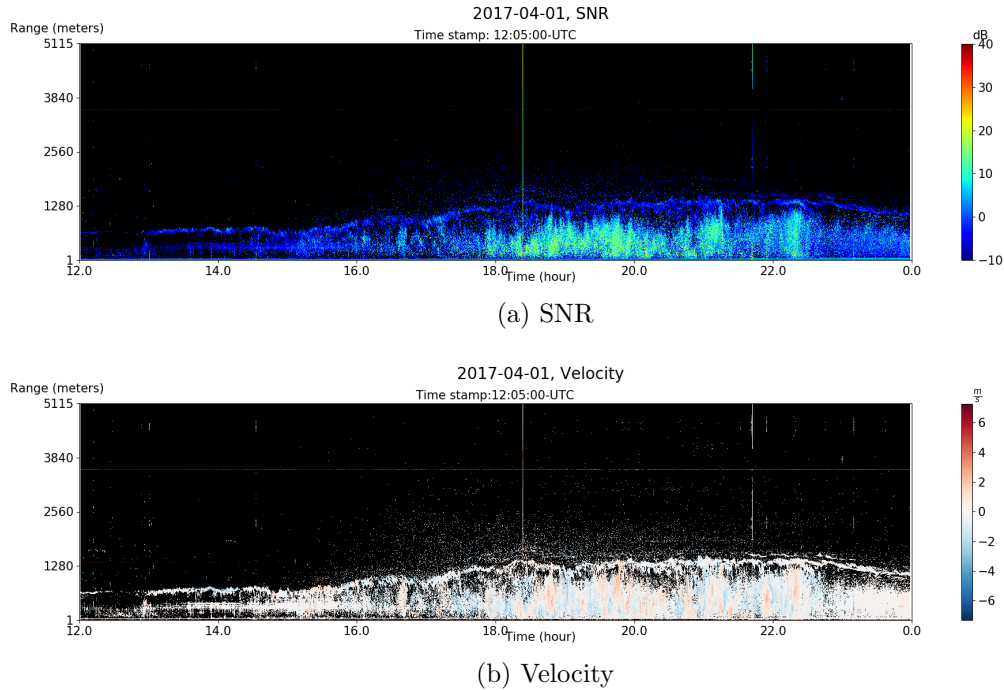


(b) Velocity

**Figure 5.2.** SNR and Velocity plots for the convective boundary layer on April 1st, 2017. Data displayed from 12 to 24-UTC.

The refractive index structure parameter is useful when viewing a convective boundary layer. Figure 5.3 shows the structure parameter for the convective boundary layer discussed above. Note the color axis for this plot has a logarithmic scale, and units of $\frac{m^3}{m^2}$. This plot spans 5 km on the vertical axis and twelve hours on the horizontal scale. The structure parameter at the top of the boundary layer is the value of interest, and in this plot peaks at approximately $10^{-14}m^{-\frac{2}{3}}$. This is a moderate structure parameter value.

Another example of a convective boundary layer is depicted in Figure 5.4. This data was collected on April 29th, 2017 from 12 to 24-UTC. From the structure parameter plot, the boundary layer is steadily increasing until 19-UTC. Afterwards, the
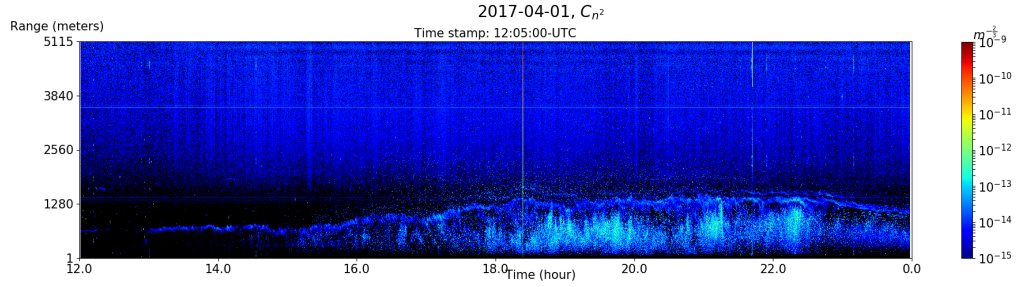
**Figure 5.3.** Refractive index structure parameter collected during a typical convective boundary layer, April 1st 2017.

boundary is difficult to identify. The peak structure parameter value at the top of the boundary layer is just above $10^{-13}m^{-\frac{2}{3}}$, higher than in the previous example.
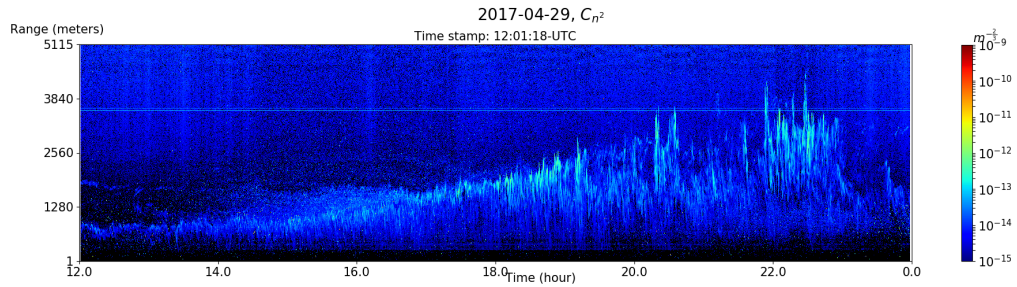


(a) Refractive index structure parameter
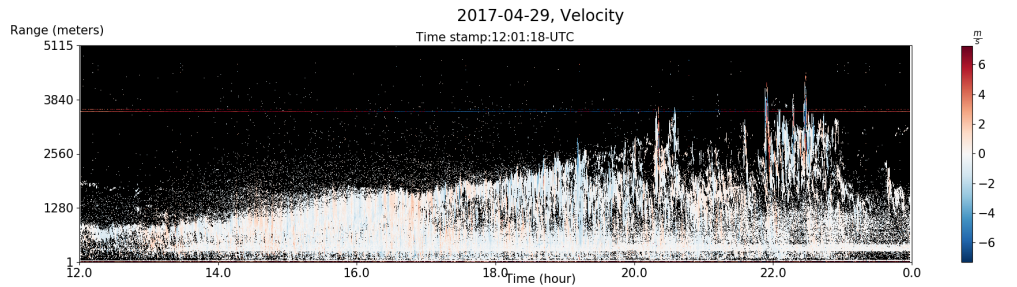


(b) Velocity

**Figure 5.4.** $C_{n^2}$ and Velocity plots for the convective boundary layer from April 29th, 2017.

A final convective boundary layer example is shown in Figure 5.5. In these plots, there are several boundaries evident in the structure parameter plot. The brightest layer represents the top of the boundary layer, and the others are likely shear layers. This is verified when looking at the velocity plot, where parcels of air are stop rising

48

at the brightest layer. There is no convection evident above that layer. The structure parameter has a peak value just below $10^{-13} m^{-\frac{2}{3}}$, indicating relatively sharp gradient in refractive index.



(a) Refractive index structure parameter
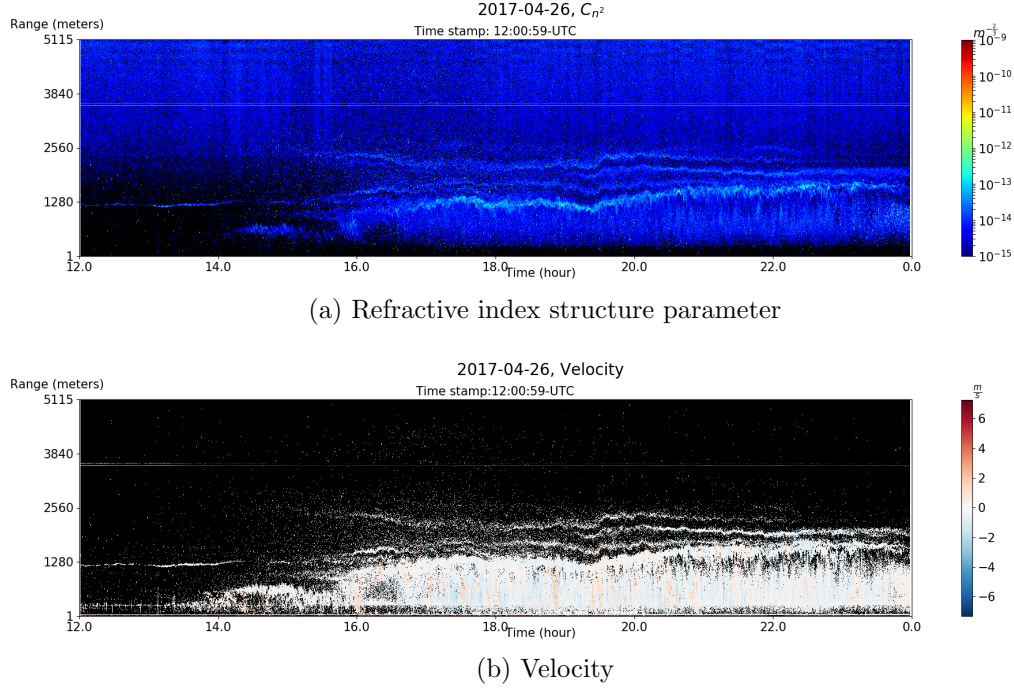


(b) Velocity

**Figure 5.5.** $C_{n^2}$ and Velocity plots for the convective boundary layer from April 26th, 2017.

## 5.2  Insects and Bird Targets

Insects and birds are a major data feature which distort other environmental data. Figure 5.6 shows SNR and Velocity from data collected on April 29th, 2017 at 2-UTC. The plot spans approximately 5 km on the vertical axis and 1 hour on the horizontal. Intensity shows the signal to noise ratio. SNR below -10 dB are set to black. Each of the dots of high SNR in the data set are likely birds or insects. The number of insects is a weak function of temperature. The velocity of insects may roughly correspond to the vertical wind speed. In this plot, there are enough insects to distort the dataset, and make it more difficult to distinguish the boundary at approximately 2 km. The

49

Doppler spectrum in Figure 5.7 shows the spectral behavior of these insects. This spectrum is from a single 16 second time bin, and spans 5 km on the vertical scale and $\pm 7.3 \frac{m}{s}$. Spectral data below -30 dB are set to black. The horizontal streaks of high signal strength at approximately 2 km, 1 km and 0.5 km are instances of insects or birds.



(a) SNR

(b) Velocity

**Figure 5.6.** SNR and Velocity data showing insects and birds, April 29th 2017, 2-UTC
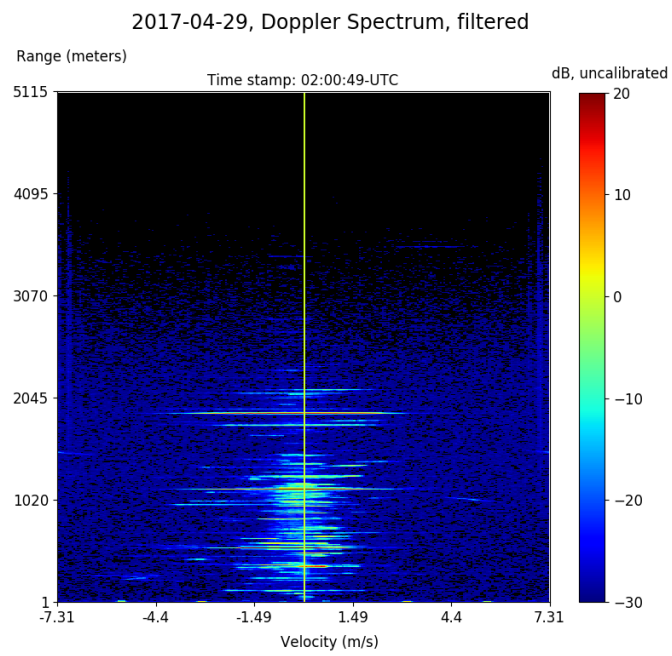
**Figure 5.7.** Doppler spectrum data showing insects and birds, April 29th 2017, 2-UTC

# CHAPTER 6

# PRECIPITATION DATA

Improved system performance for VORTEX-SE allows characterization of light precipitation events. Sensitivity is traded for a higher receiver saturation power, such that the system can measure stronger rain events. Increased velocity range for the 2017 deployment allows the system to measure typical rainfall velocities unambiguously. Deliverable results include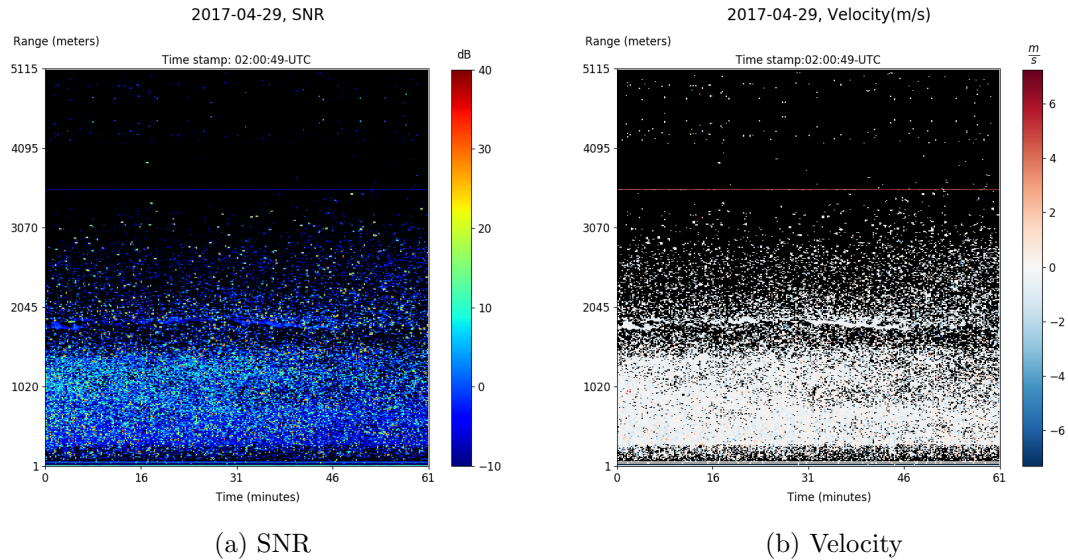 Reflectivity Factor and velocity as a function of height and time. The Drop Size Distribution (DSD) of rain events is another parameter of interest. DSDs are estimated from spectral reflectivity factor data. That is, the Doppler Spectrum of Reflectivity factor. These estimates are biased by any vertical winds that may be present.

This chapter begins by illustrating typical behavior of rain data evident during the experiment. Some examples of DSD estimates are also performed to demonstrate relevant characteristics. The possibility of extracting the wind bias from spectral data is explored in this section. Finally, an analysis is performed on the two longest rain events from 2017 in order to assess the validity of estimated DSDs. This is done by comparing directly measured reflectivity factor to that obtained from the estimated DSDs, and an approximate relation between Z and rainfall rate R (the Z-R relation).

## 6.1   Rain data

Similar to viewing the system spurious response, the Doppler spectrum is useful for viewing instantaneous rain data. An example from a rain event on April 30th, 2016 at 0-UTC is depicted in Figure 6.1. This spectrum spans the 5km range in

the vertical scale. The horizontal scale represents velocity in $\frac{m}{s}$, with a negative downwards reference. During the 2016 deployment, the velocity axis spans from $\pm 5 \frac{m}{s}$. The magnitude is calibrated in terms of dBZ per velocity bin.
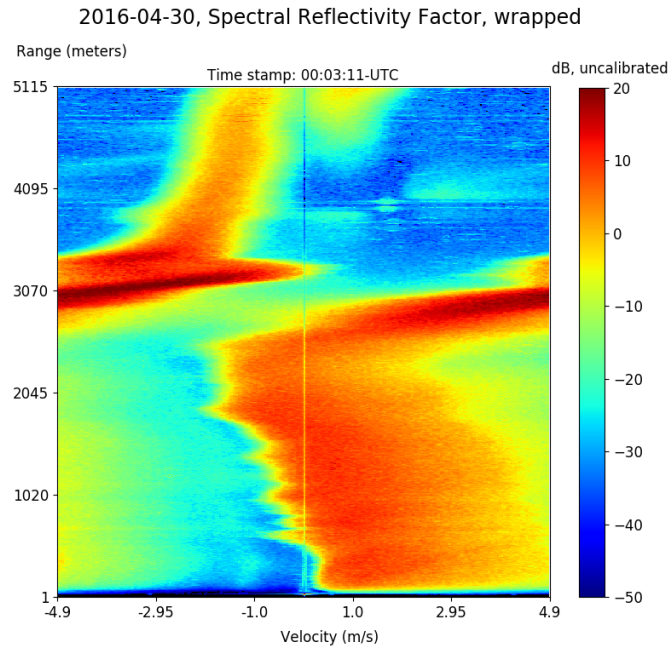


**Figure 6.1.** Example of wrapped spectral reflectivity factor in light rainy conditions, from April 30th, 2016

Several data features are evident in this plot. System spurious products are evident at approximately 3.5km. The streak of high reflectivity across the velocity dimension at approximately 3km is the melting layer. Above the melting layer, water particles are frozen and falling slowly, appearing near the zero Doppler bin in the top-middle of the plot. As the drops melt, they have a higher reflectivity than frozen particles above, and larger cross sectional area than drops below. This in addition to an increased drop density is why the melting layer has a relatively high reflectivity. Below the melting layer drops are falling much faster. Drops falling faster than the system unambiguous velocity range will wrap around the plot and appear on the right-hand side as opposed to the left-hand side. Drop velocities twice as big as the unambiguous

system velocity range will alias over the zero Doppler bin, and be more difficult to unwrap.

Another feature evident in the plot manifests as a small increase in spectral reflectivity factor at approximately -1 $\frac{m}{s}$ in the lowest 500 m. This feature is possibly a reflection from vertical wind, or possibly a system sidelobe. Properties of each of these data features will be discussed later in this Chapter. This effect is clearer when viewing the plot animated over time.

Velocity and reflectivity factor plots are useful for looking at rain data over time. Reflectivity factor plots are constructed as a summation of the Spectral Reflectivity Factor data over the velocity dimension. Velocity plots are found using the same method previously discussed. Figure 6.2a shows a plot of velocity data collected over one hour on April 30th, 2016 at 0:00-UTC. The corresponding reflectivity factor measurements are shown in Figure 6.2b. Both of these plots span 5 km on the vertical axis and 1 hour on the horizontal. Several rain features are evident from these plots. The melting layer is visible just above 3 km, as a layer of high reflectivity, or a sharp gradient in velocity. This rain data was collected during a moderate rainfall.

Raindrops start falling below the melting layer, the velocity plot shows a high downward velocity for most of these drops. Where the velocity changes from downward to upward, it is assumed that the measurement is aliasing. The effect of aliasing is most evident when looking at the Doppler spectrum.

During the 2016 deployment, a significant amount of aliasing was evident in the data-set. This was the motivation to increase the velocity interval for the 2017 deployment. Data which aliased twice proved difficult to consistently unwrap, and likely obscured vertical wind data which would otherwise be visible.

One important consideration when viewing precipitation data collected during VORTEX-SE is the calibration method used. The noise floor is estimated from a median of received power in the instantaneous Doppler Spectra, and thresholded based

(a) Velocity          (b) Reflectivity Factor
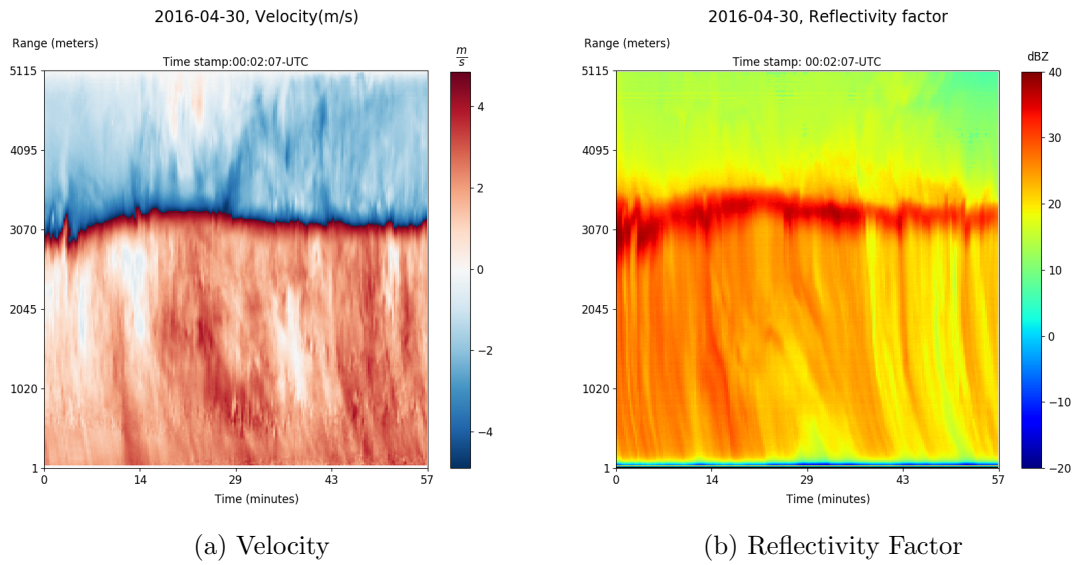
**Figure 6.2.** Example of velocity and reflectivity factor in moderate rainy conditions, from April 30th 2016 at 0-UTC

on the terminated input measured noise power. Under conditions where received power is consistently high, as in most precipitation cases, the noise power is set to the terminated input noise power. Figure 6.3 shows the noise floor estimate which corresponds to the velocity and Reflectivity factor plots previously discussed. The noise floor is reset for the duration of this plot. The exception is the few spots of higher power in the top km of the plot.

As an example of reflectivity and velocity data collected during the 2017 deployment at 15-UTC on April 3, is depicted in Figures 6.4b and 6.4a. The reflectivity plot shows this was a very light rain event. Light aliasing is evident in the velocity plot, at the discontinuity where the color changes from dark blue to dark red. Compared to data collected in 2016, much less aliasing occurs due to increased velocity range. The melting layer is clearly evident just below 3 km as the band of high reflectivity. Above the melting layer frozen particles of lower reflectivity are evident as falling slowly; and below it rain starts to fall at its terminal velocity.
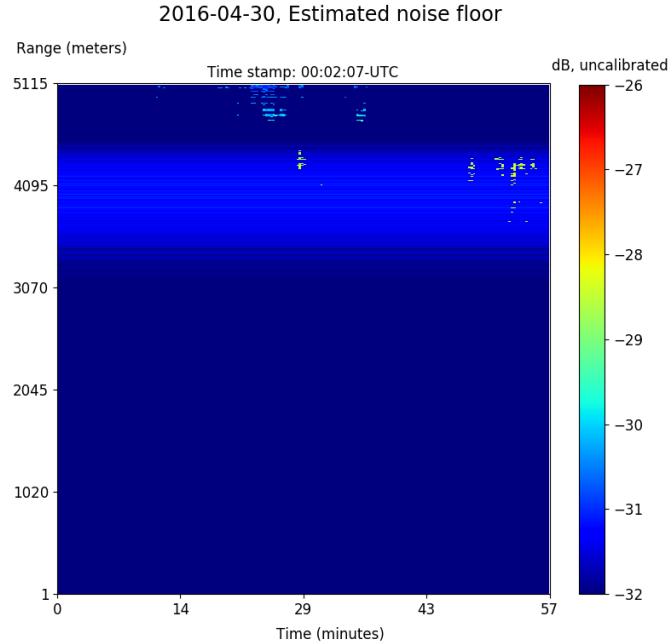
**Figure 6.3.** Example of the noise floor estimate in moderate rainy conditions, from April 30th 2016 at 0-UTC

As with the previous example, it is important to keep the noise floor estimate in mind when examining this data; the noise floor is depicted in Figure 6.5. In this case, returns are large enough that data is thresholded in the lower half of the plot. Unlike the previous example, there is a large portion towards the top of the plot where the data is not high enough in magnitude to exceed the threshold. This causes an apparent discontinuity in the noise estimate as a function of height. These discontinuities bias the Doppler Spectrum, and all parameters calculated from it.

Figure 6.6 shows a snapshot of the wrapped spectral reflectivity factor from the April 3rd, 2017 rainfall event. As previously discussed, data collected during the 2017 experiment has an expanded velocity range of $\pm 7.3 \frac{m}{s}$ on the horizontal axis. The effect of the estimated noise floor discontinuity discussed above is evident in this case. Where the noise floor estimate was reset, the Spectral Reflectivity is biased higher; and where the estimate was not thresholded the Spectral Reflectivity is lower.

(a) Velocity                                    (b) Reflectivity Factor

**Figure 6.4.** Example of Velocity and Reflectivity Factor in light rainy conditions, from April 3rd 2017
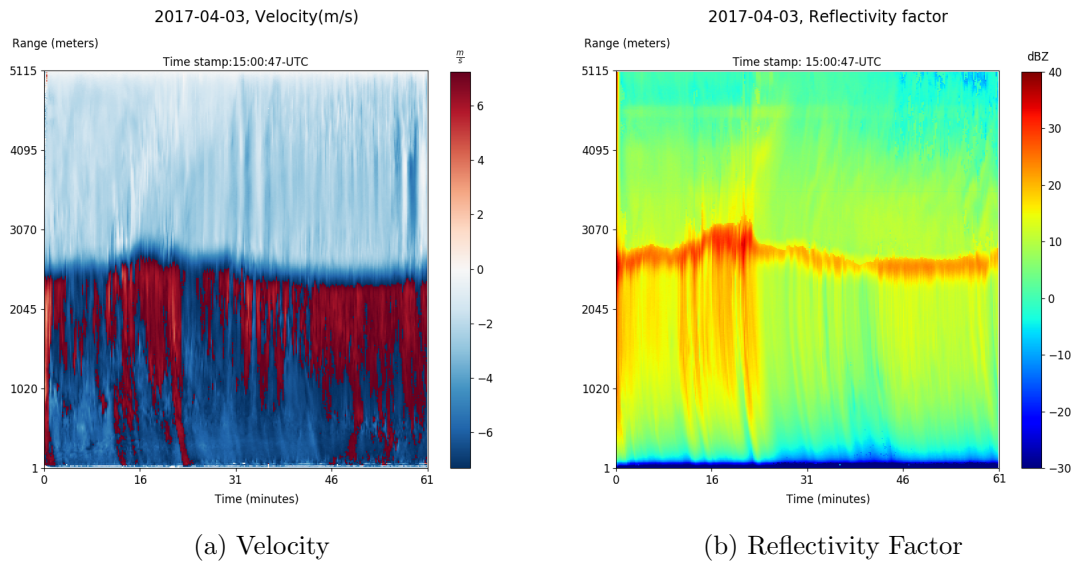
In this case, the noise floor estimate is completely reset for ranges where rain is falling. This is necessary so rainfall does not bias the noise floor estimate very high, and lead to artificially low SNR and Reflectivity values. The problem with this approach is that it does not account for drift or changes in the noise floor over time. As such, the calibration is not as accurate in rainy conditions.

Figure 6.7 shows the averaged spectral reflectivity factor from April 22nd, 2017 at approximately 22:30-UTC. This figure displays two features of interest. The first is clear-air scatter evident surrounding the zero velocity bins. This tends to exhibit clear-air behavior covered in Chapter 5, however this signal is relatively weak compared to rain and is often overwhelmed by it. The velocity measured for clear air in this case is very low, however it will bias the drop size distribution estimate discussed in the next section. Direct observation of clear-air scatter as in this case can be used to correct the vertical wind bias in DSD estimates.

The second feature evident in Figure 6.7 is a system sidelobe which appears as a bump of high reflectivity at approximately $-11\frac{m}{s}$. This second feature is interesting

57
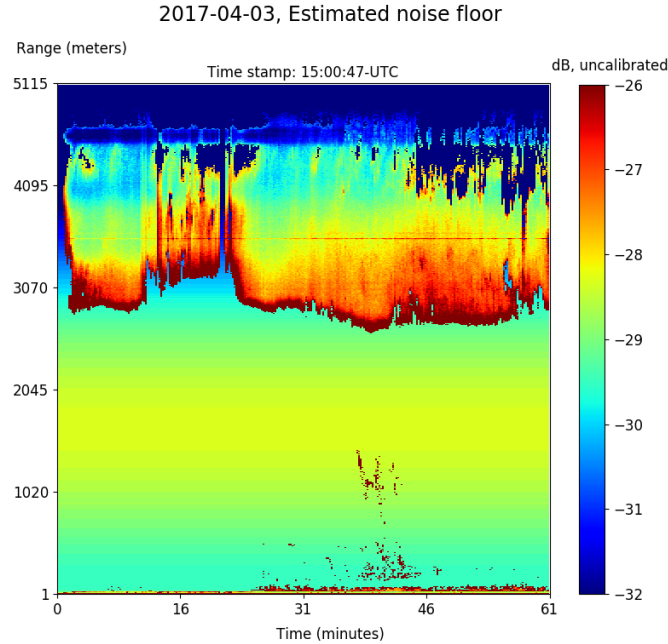
**Figure 6.5.** Example of estimated noise floor in light rainy conditions, from April 3rd 2017

because it manifests behavior similar to clear-air scatter; most notably in its volume distribution characteristics. The cause of this feature is unknown; though its behavior suggests it is some sort of system sidelobe. It is referred to as a sidelobe herein for lack of a better description. When this feature falls within the velocity range in which vertical winds usually fall, it is not clearly distinguishable from clear-air scatter.

A cross sectional view of this plot at a height of 400 meters is in Figure 6.8. The clear-air signal manifests in this plot as a bump surrounding the zero-velocity point. The two sharper lines immediately surrounding the zero velocity bin is are system characteristic. The sidelobe is evident in the data at approximately $-11\frac{m}{s}$. These sidelobes then to occur when a sharp gradient across the velocity dimension is present. In the instantaneous spectrum, it is clear that the sidelobe shape matches that of the sharp gradient closely.
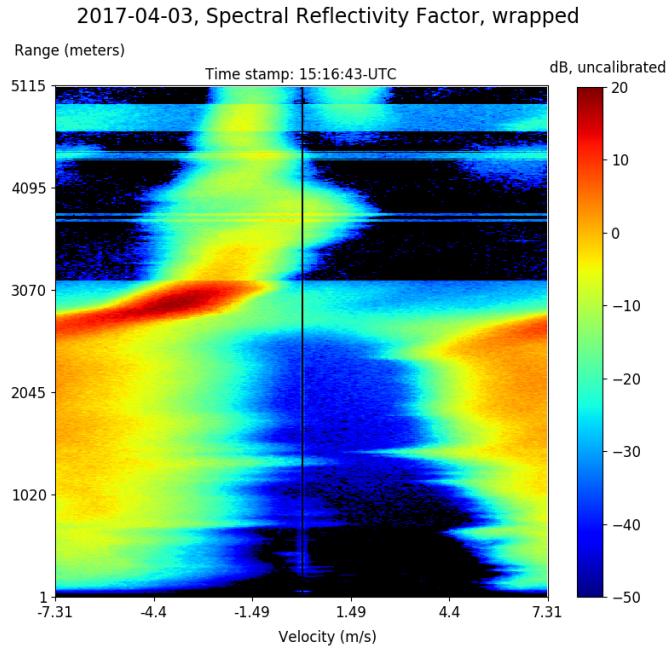
**Figure 6.6.** Example of the wrapped spectral reflectivity factor in light rainy conditions, from April 3rd 2017

In 2017 data, this feature typically falls outside of the velocity range expected on vertical winds. 2016 data is prone to this feature falling within the expected vertical wind bias range, which adds ambiguity to potential corrections. This is evident in Figure 6.1 from the beginning of this Chapter, where the reflectivity bump evident at low ranges and velocities could be representative of either of these characteristics. In the animated spectrum this characteristic traces the behavior of the largest raindrops, so is more likely a sidelobe than a clear-air echo.

To better understand the variation of rain events over time, it is useful to look at a longer rain event. Figure 6.9 shows the reflectivity factor collected during a six hour rain event on April 3rd, 2017. The corresponding velocity is shown in Figure 6.10. Fluctuations in reflectivity and velocity are evident throughout the event. There is a break in the rainfall at approximately 14-UTC. The most intense rainfall is evident just after 10-UTC, and a longer period of moderate rainfall occurs at 13:30-UTC.
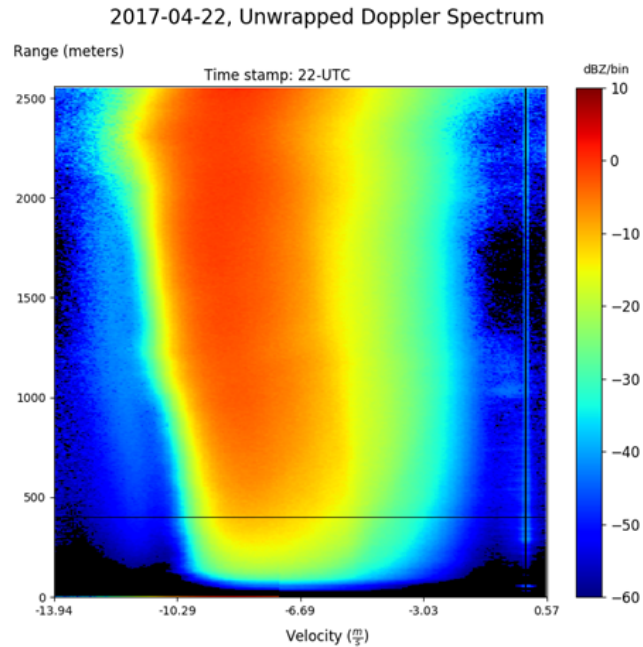
**Figure 6.7.** Reflectivity factor data with evident system sidelobe and vertical wind bias, from April 22nd 2017

Velocity aliasing is evident for the majority of the event, however no twice aliased data occurs. The noise floor estimate for this time period is shown in Figure 6.11. From this plot, it appears that the terminated input measured noise floor is used to calibrate most falling rain. Most data above the melting layer and in light mists are calibrated with the median spectral value.

Figures 6.12 and 6.13 show reflectivity factor and velocity for the rain event spanning from March 25th, 2017 at 23-UTC to March 26th, 2017 at 5-UTC. The noise estimate is depicted in Figure 6.14. Again, fluctuations in reflectivity and velocity throughout the event are evident. Reflectivity is generally lower in this example than in the previous one. Velocity aliasing still occurs, but again not as much as in the previous example. There are two periods where the rainfall lets up enough that the median noise estimate is selected; occuring after 23-UTC on the 25th and after 4-UTC on the 26th.
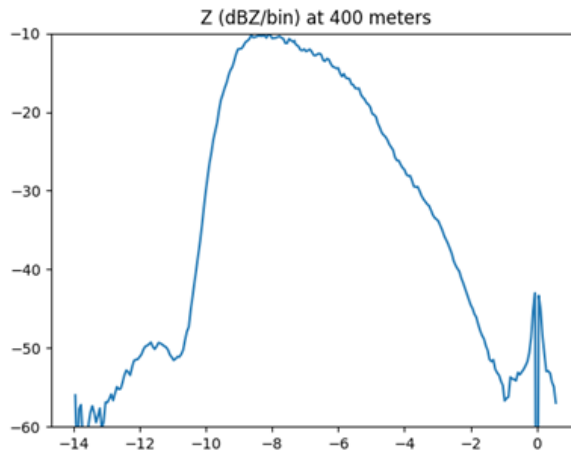
**Figure 6.8.** Reflectivity factor data with evident system sidelobe and vertical wind bias, from April 22nd 2017
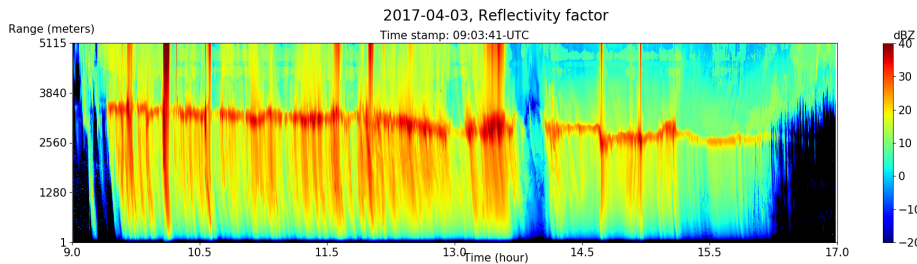


**Figure 6.9.** Reflectivity factor spanning the rain event on April 3rd, 2017.

## 6.2 Drop Size Distribution Estimates

The approach for estimating the drop size distribution is described in Chapter 2. The instantaneous spectral reflectivity factors measured in 16 second intervals, are unwrapped and averaged over twenty time frames, or a five minute period. This averaging is performed to smooth instantaneous fluctuations in rainfall and mitigate any vertical wind bias which may be present and near-zero. Estimates from data collected during the 2017 campaign are presented in this section, due to higher reliability of unwrapping the Doppler spectrum. The expanded system velocity range during the
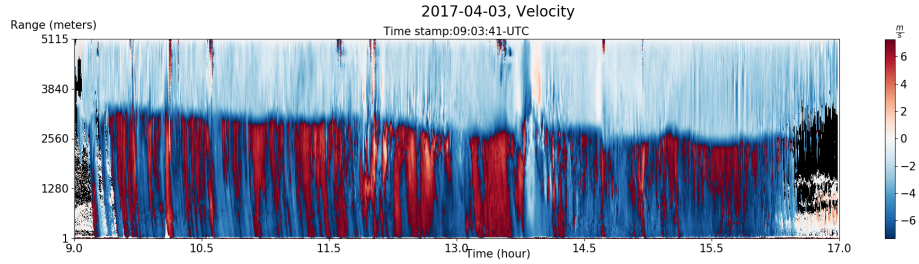
**Figure 6.10.** Velocity spanning the rain event on April 3rd, 2017.
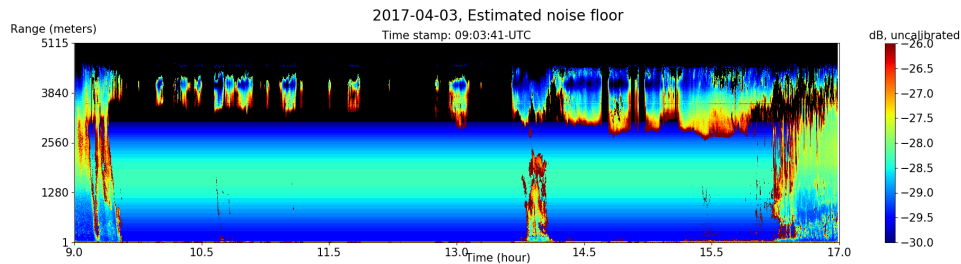


**Figure 6.11.** Noise Estimate spanning the rain event on April 3rd, 2017.

2017 deployment also makes it possible to distinguish between vertical winds and system sidelobes in light and moderate rainfall.

Estimating the drop size distribution begins by averaging the Doppler Spectrum over a 5 minute period. An example of this averaged Doppler Spectrum during a very light rain event is shown in Figure 6.15. This data was collected on April 3, 2017 during the five minute period beginning at 13:24-UTC. The vertical axis in this plot represents range in meters, up to 2.5km. Data above this height is neglected as it does not include significant rainfall. The horizontal axis represents velocity, negative downwards in $\frac{m}{s}$. This Doppler spectrum has been unwrapped by assuming all positive velocities are aliased. The magnitude of this plot is Spectral Reflectivity Factor in dBZ.

A cross section of this wrapped spectral reflectivity plot which corresponds to the horizontal line at approximately 450 meters is plotted in Figure 6.16. The cross section is plotted as reflectivity in dBZ versus velocity in $\frac{m}{s}$. One feature evident in
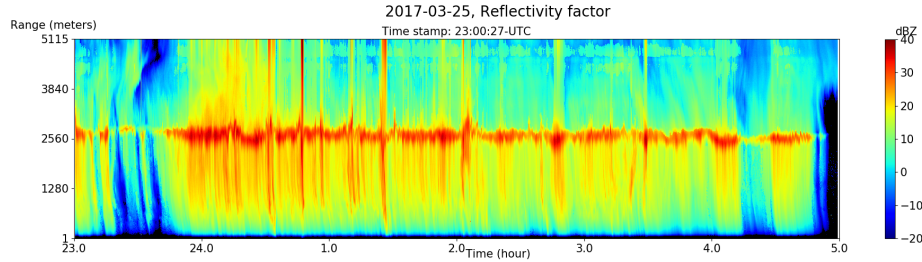
**Figure 6.12.** Reflectivity factor spanning the rain event on March 26, 2017.
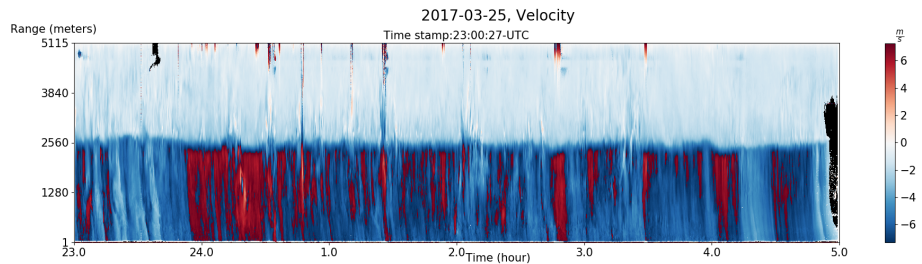


**Figure 6.13.** Velocity spanning the rain event on March 26, 2017.

this plot is an apparent noise floor of 0 dBZ across velocities. For comparison, Figure 6.8 shows data down to -55dBZ/bin. This 0dBZ is not the noise floor, but an artifact of rainfall and forcing the noise estimate to a previously measured value. This feature is typical in light to moderate rain conditions, and varies in level with rain intensity; it also tends to overwhelm any clear air scatter which could be detected. The rainfall is visible above this bias for velocities between approximately $-4\frac{m}{s}$ and $-10\frac{m}{s}$. The characteristic of Z increasing with increasing velocity is typical. The fastest falling drops are the largest, even though there are relatively few of them they contribute the most to reflectivity. This is because reflectivity is a function of drop diameter to the sixth power. A relatively sharp gradient is typical below the largest drops, in this case occuring at approximately $-10\frac{m}{s}$.

Figure 6.17 shows the DSD estimated from data collected on April 3, 2017 in the five minute period beginning at 13:24-UTC. The vertical axis is on a logarithmic scale from $10^2$ to $10^6$, and represents the number of rain drops per unit volume. The hori-
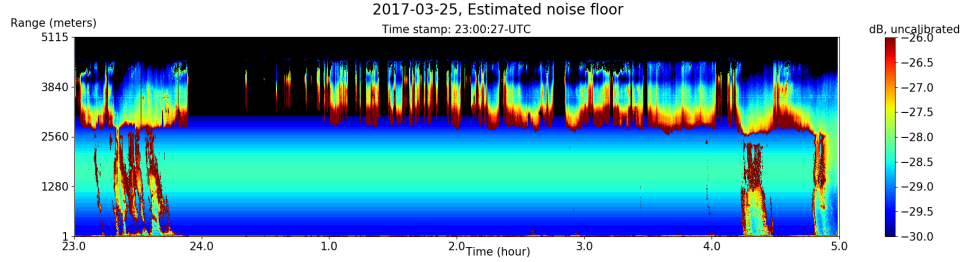
**Figure 6.14.** Velocity spanning the rain event on March 26, 2017.

zontal axis in this plot represents rain drop diameter in millimeters. The horizontal axis in this plot is limited to 5mm, as there are not typically a significant number of larger drops. Spectral reflectivity data for each time bin during this period was unwrapped by assuming all positive velocities contain aliased data. Data above 2.5 km was truncated in order to neglect the melting layer. The change in parameters and normalization were performed to convert spectral reflectivity to the number density. The Figure displays a cross section of the number density at a height of 150 meters as a blue line. The orange line is included for comparison, and represents the ideal Marshall-Palmer distribution for theoretical results. The blue curve is a linear factor of approximately three times higher than the orange curve. [10]

In order to validate the resultant drop size distribution, Reflectivity factor is estimated from it and compared to the measured reflectivity. The measured reflectivity is calculated by summation of spectral reflectivity across the velocity dimension at the height bin of interest. Estimated reflectivity is found by calculating rain rate from the DSD, and then using the Marshal-Palmer relation to approximate Z.

| Rain rate | $0.097 \frac{mm}{hr}$ |
|---|---|
| Measured Reflectivity | 19.81 dBZ |
| Estimated Reflectivity | 6.83 dBZ |
| Reflectivity error | 12.98 dB |

**Table 6.1.** Reflectivity data calculated from the April 3, 2017 DSD at 15-UTC and a height of 150 meters

64

**Figure 6.15.** Example of averaged, unwrapped spectral reflectivity factor during a very light rain, collected over a five minute period on April 3, 2017 at 13:24-UTC

This reflectivity comparison for the spectral reflectivity discussed above are summarized in Table 6.1. It appears there is a 13dB bias in the estimated reflectivity, compared to the measured value. Many factors likely contribute to this bias, including imperfect absolute calibration, possible vertical wind biases, and errors introduced by the approximate nature of the equations used for calculation. An analysis of a long rain event is performed at the end of this chapter to better quantify the relation between these estimated and measured reflectivity values.

A few more DSD estimates will illustrate typical results, and demonstrate the behavior of environmental effects which impact the data. The example in Figure 6.18 was collected on March 26, 2017 at 2:33-UTC, and illustrates a clear vertical wind bias. The left hand side of the spectral reflectivity plot shows familiar signs of vertical wind biases- as a distributed volume target above the rainfall. The cross sectional plot shows a corresponding bump in reflectivity at approximately zero velocity. This

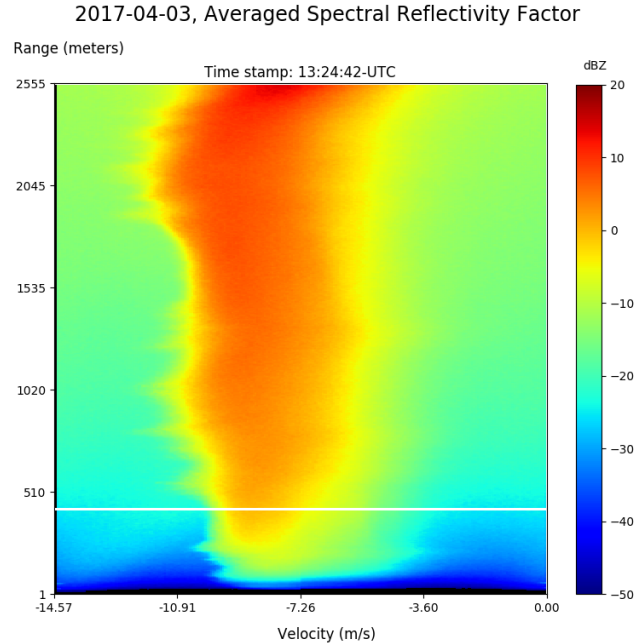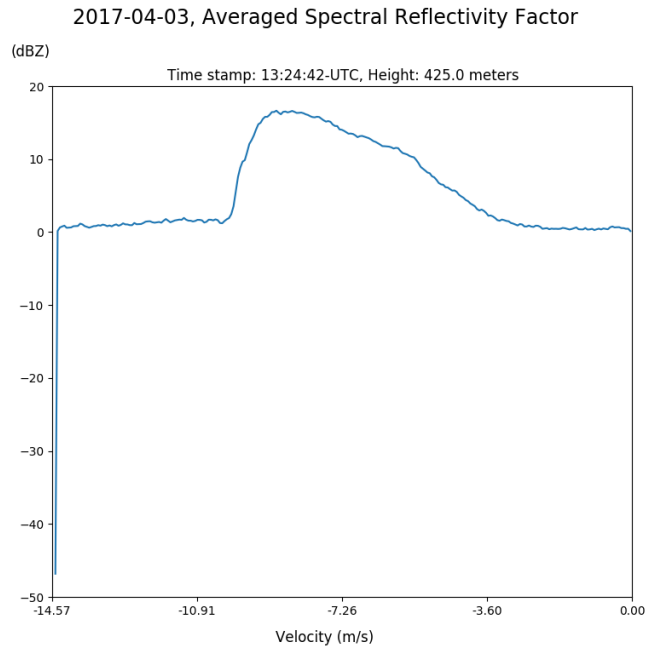**Figure 6.16.** Cross section of averaged, unwrapped spectral reflectivity factor during a very light rain, collected over a five minute period on April 3, 2017 at 13:24-UTC

is notedly distinct from a system sidelobe since it occurs far in velocity from the largest raindrops and the gradient across the velocity dimension is not very large. It is also clear from the cross sectional plot that rain is artificially raising the reflectivity factor noise floor for this measurement.

The next example is from data collected on March 26, 2017 at 3:07-UTC. Figure 6.19a shows the spectral reflectivity factor averaged over this five minute period, and Figure 6.19b shows the cross section taken at 750 meters. In the spectral plot, there are clear indications of insects at approximately -0.5 $\frac{m}{s}$, most notably in the lowest km. The cross sectional plot shows a sharp bump of high reflectivity, which corresponds to these insect returns. The artificial noise floor is high enough in this case that direct observation of vertical wind biases cannot be directly measured. This is also true in most cases of higher reflectivity rainfalls; the noise floor overwhelms any scattered signals from air. For the purposes of this Chapter, it is assumed that
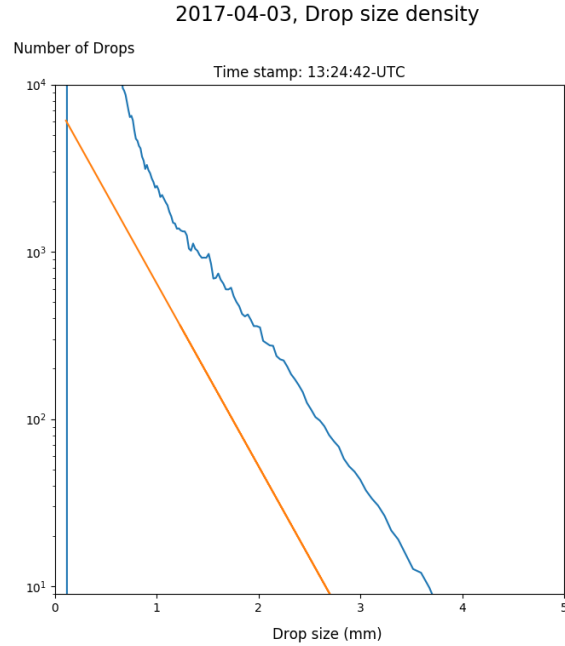
**Figure 6.17.** Drop size distribution estimated during a very light rain, collected over a five minute period on April 3, 2017 at 13:24-UTC

in rainy conditions insect velocity can not be used to correct vertical wind velocity bias in the DSD.

The DSD estimate in Figure 6.20 shows an example of the system sidelobe which appears in certain rain data. This feature is evident in the reflectivity cross section plot as a bump in the noise floor at approximately -10$\frac{m}{s}$. It appears in the spectral reflectivity plot as a bump of reflectivity spanning height in the neighborhood of the same velocity. In the spectral plot, this bump roughly traces the largest raindrops with a velocity offset. This is most evident when the instantaneous reflectivity plot is animated to show the behavior of these sidelobes over time.

To better quantify the relation between measured and estimated Z and assess the validity of drop size distribution estimates, it is necessary to look at a larger sample size. Data used for this analysis is of the same form as in Table 6.1. To start, measured and estimated reflectivity factor data covering each five minute period over the time

(a) Spectral Reflectivity

(b) Reflectivity Cross Section



(c) Reflectivity Cross Section

**Figure 6.18.** Example of vertical wind bias evident in DSD estimate, collected over a five minute period starting on March 26, 2017 at 2:33-UTC

span depicted in Figure 6.9 is examined. This corresponds to the longest continuous rain event during the 2017 deployment. Data where Measured Reflectivity are below 3dBZ are ommitted. A height of 150m was selected to demonstrate results.

Figure 6.21 is a plot of measured versus estimated reflectivity factor collected during the April 3, 2017 rain event, and includes 84 data points with no corrections applied. The horizontal axis shows measured reflectivity factor and the vertical axis is estimated reflectivity factor, both in dBZ. A trendline showing the best-fit linear relation between estimated and measured values is included as a blue dashed line.

(a) Spectral Reflectivity
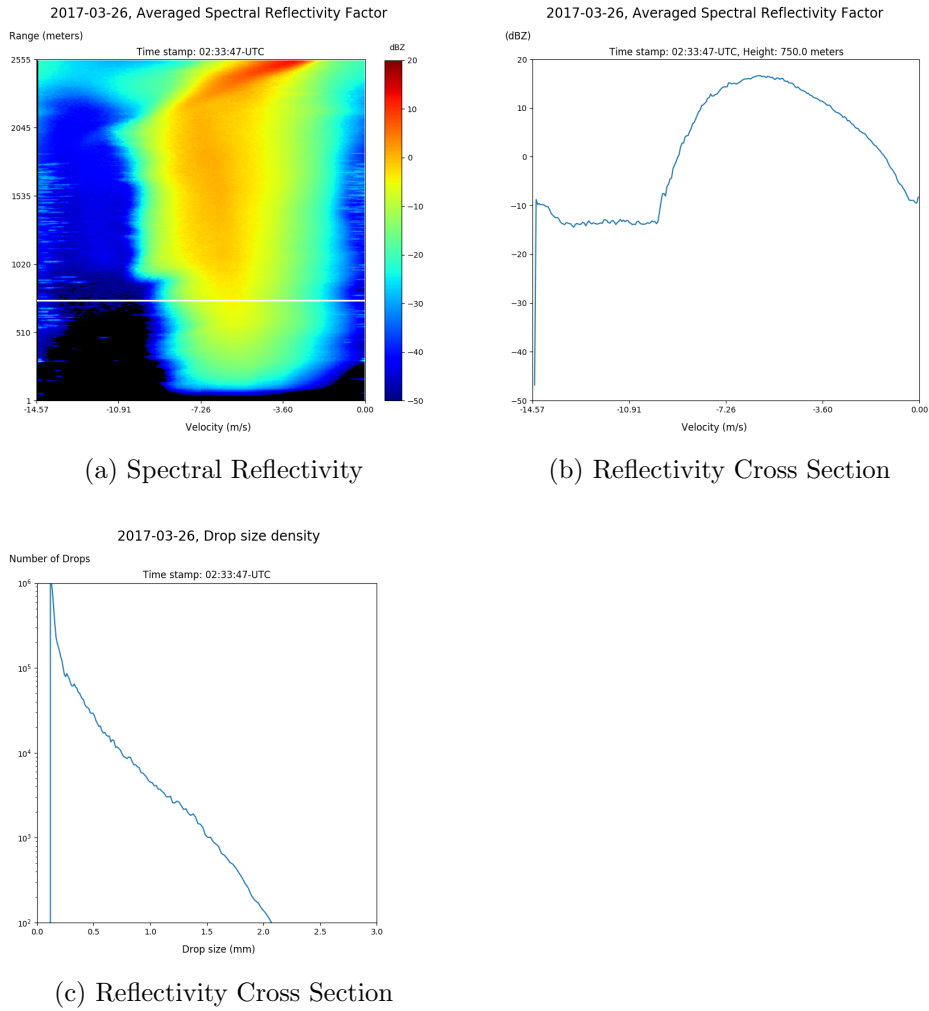
(b) Reflectivity Cross Section



(c) Reflectivity Cross Section
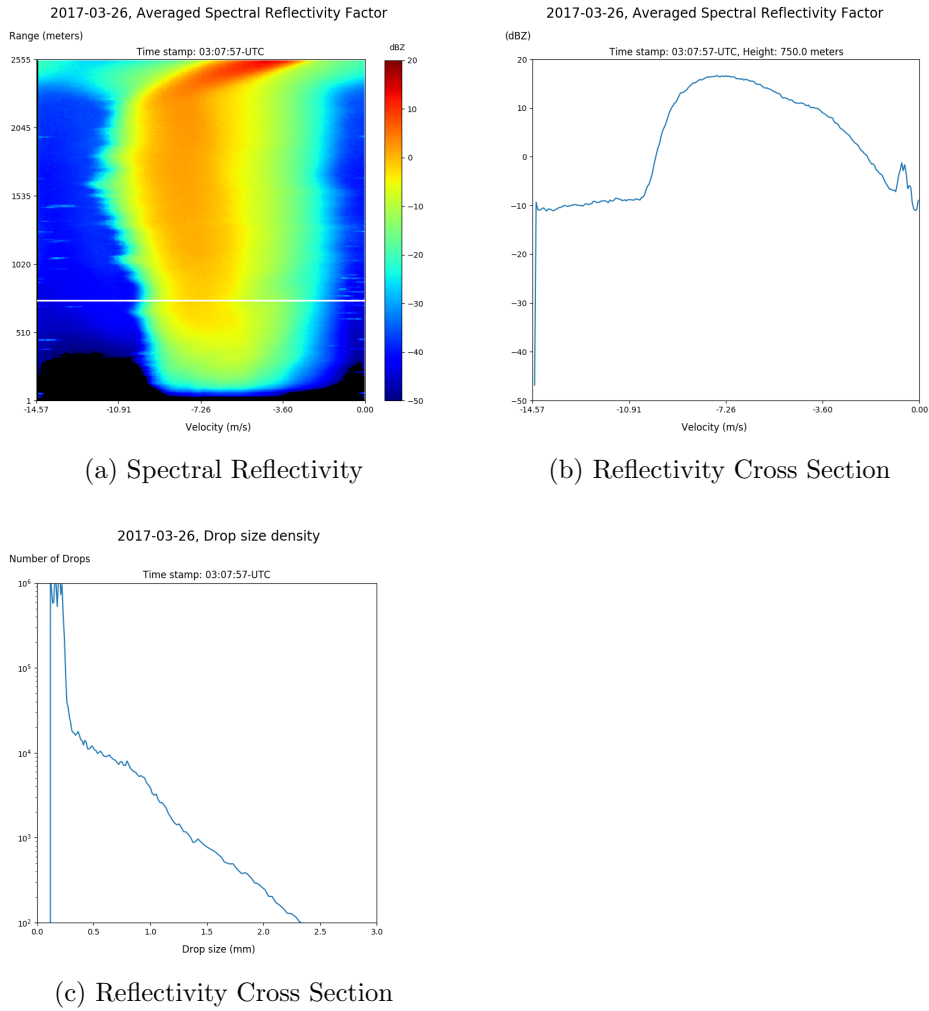
**Figure 6.19.** Example of insects evident in DSD estimate, collected over a five minute period starting on March 26, 2017 at 3:07-UTC

The equation which constitutes this line appears in the top right hand corner of this plot. This line has an apparent slope of 1.2, and intercept of approximately 16dB. The intercept of this line suggests that there is a significant bias between estimated and measured data, as first shown in Table 6.1.

To examine how well data points fit the trendline in this figure, a a histogram of residual values is constructed in Figure 6.22. This plot shows a significant number of points which deviate from the trendline by more than 3dB. The behavior of the

(a) Spectral Reflectivity

(b) Reflectivity Cross Section



(c) Reflectivity Cross Section
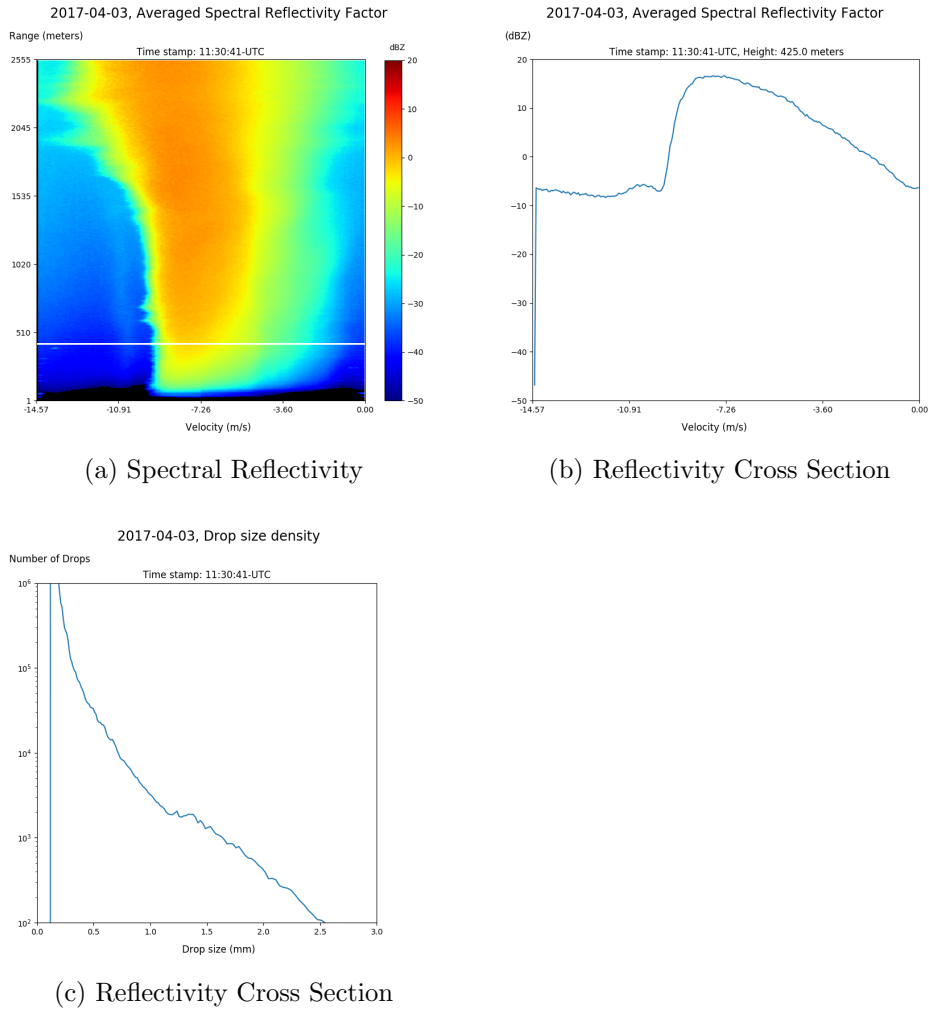
**Figure 6.20.** Example of a sidelobe evident in DSD estimate, collected over a five minute period starting on April 3, 2017 at 11:-UTC

trendline and histogram are not sufficient to justify correlation between estimated and measured results.

One major source of error which was not corrected in the previously discussed analysis is for vertical wind bias. To see if vertical wind biases are a major source of error in the assembly of information previously discussed, the same analysis is repeated using data which is corrected for vertical wind biases. For this analysis, wind biases were approximated on a conservative basis for this analysis. There are some cases where the wind bias is evident and some where a wind bias is extrapolated

**Figure 6.21.** Estimated vs measured Reflectivity factor for each five minute period during the April 3rd, 2017 rain event.
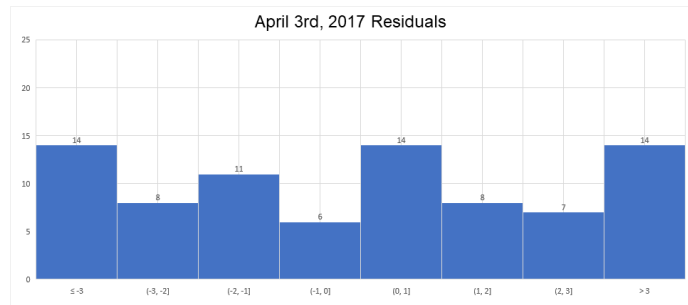


**Figure 6.22.** Distribution of residuals for rain event on April 3, 2017.

from other heights or from individual (non-averaged) spectra. In instances where there is little evidence of vertical wind bias, no correction is performed. In ambiguous cases where features are evident of different or conflicting wind biases, no correction is performed. There are many times where a vertical wind is potentially present, but contaminated by rain echo in heavy rain conditions.

Figure 6.23 plots estimated versus measured reflectivity factor for each time period sampled, corrected for vertical wind speed as appropriate, and shows the trendline which approximates the relation. Orange open circles in this plot represent the original uncorrected data, while blue closed circles represent data corrected for vertical wind bias. The trendline for corrected data is indicated as a blue dashed line, and the

71

equation of this line is included in the top right hand corner of the plot. This trend-line has a slope within one percent of unity, and slope intercept of 12.6dB. Assuming this line accurately characterizes the relation between estimated and measured values, the unity slope implies a 1:1 relation between them, the intercept suggests an approximate 12.6dB bias in the estimated results.
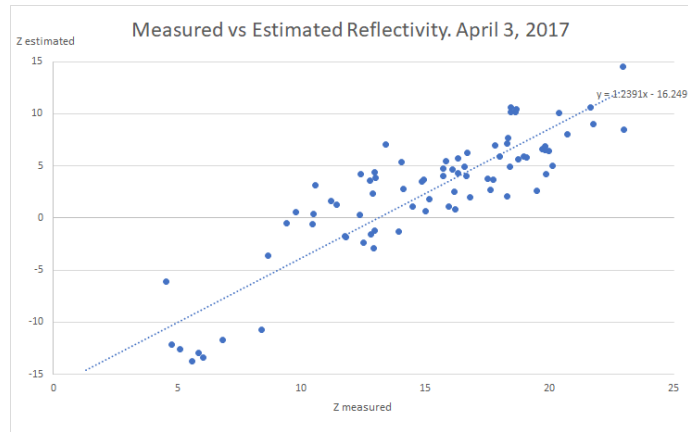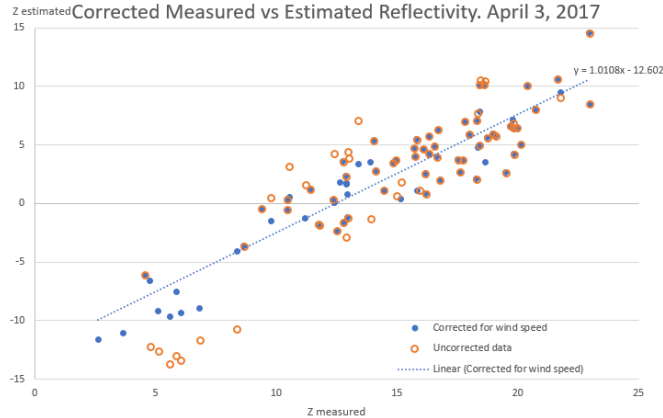


**Figure 6.23.** Estimated vs measured Reflectivity factor for each five minute period during the April 3rd, 2017 rain event. Estimated reflectivity was corrected for vertical wind biases.

Figure 6.24 is a histogram of residuals to show the deviation of data from the trendline in Figure 6.23. The horizontal axis consists of residual bins of 1dB width from -3 to 3dB, and the vertical axis represents how many data points fall in the corresponding bin. This histogram shows better correlation of data to the trendline than in the non-corrected case.

To check if these results are consistent across rain events, a similar analysis was performed on the rain event from March 26th, 2017. This was the second longest continuous rain event during the 2017 deployment. Data was again processed in 5 minute intervals and viewed at range bin 150 across the event. The event begins just after 23:00-UTC on March 25th, 2017 and ends just before 5-UTC on March 26th, 2017. For this analysis, a best-case analysis of correction was performed. This includes wind corrections previously described, but has a lower standard of evidence
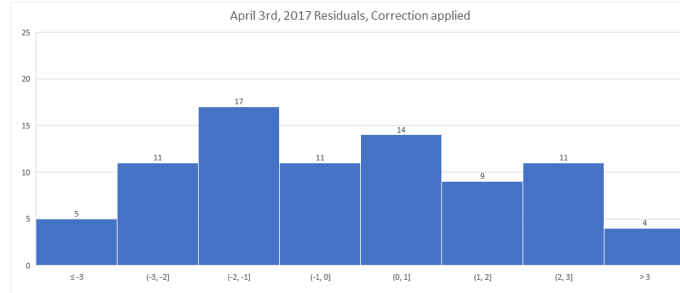
**Figure 6.24.** Distribution of residuals for corrected data from the rain event on April 3, 2017.

for determining if a feature indicates a vertical wind bias. For example, ambiguous of evident features are corrected for best results. Only features which could suggest the presence of vertical winds are used to correct the data.

Figure 6.25 shows the plot of estimated versus measured reflectivity factor from 64 data points processed from the March 26th rain event. Open orange circles represent data without vertical wind bias corrections, while closed blue circles represent data with said corrections. A best-fit linear trendline and corresponding equation is included for the corrected data in the estimated versus measured data plot. This line has a slope within five percent of unity, and a bias of approximately 12.2dB.



**Figure 6.25.** Estimated vs measured Reflectivity factor for each five minute period during the March 26, 2017 rain event.

73

Figure 6.26 shows the histogram distribution of residuals for corrected data. As in the April 3rd example, applying corrections of vertical wind biases significantly improves the distribution.
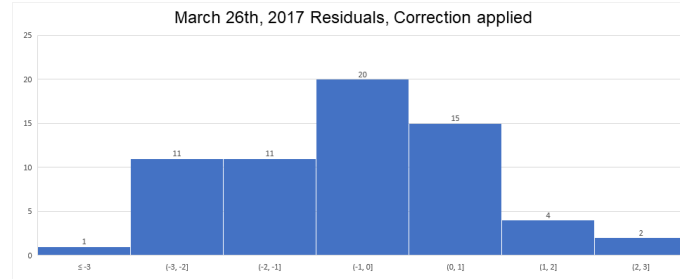


**Figure 6.26.** Distribution of residuals for rain event on March 26, 2017.

These two examples illustrate the relation between measured and estimated reflectivity factor. Looking at other various DSD results throughout the experiment, one finds that thes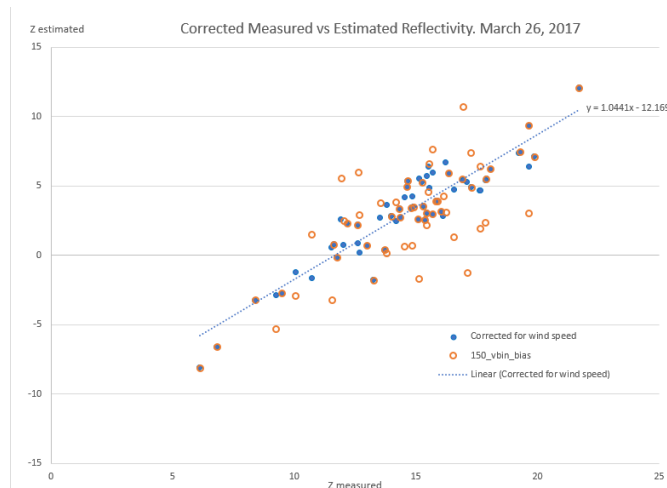e examples are roughly representative of the dataset. In other words, the bias between estimated and measured reflectivity seem to follow a trend of being approximately 12.5dB after vertical wind correction. There are of course many instances where wind bias is not evident; it is unknown if there is vertical wind present in these cases or not.

One source of this bias between Reflectivity measurements is likely errors in instrument calibration. To identify the accuracy of the calibration, it is necessary to compare results to those collected from other instruments. The local NEXRAD radar is an S-Band radar located at Hytop, Alabama; this instrument scanned directly over the FMCW observation volume during the 2017 deployment. The April 3rd, 2017 rain data in this chapter is used for comparison. Data collected from the NEXRAD radar are 15 minute base reflectivity short range data collected at 0.5 degree elevation at the longitude and latitude of the FMCW instrument. Based on the distance between instruments, relative altitude, and the elevation angle; the observation height difference between radars is approximately 400 meters.

Figure 6.27 shows the comparison of Reflectivity Factor data for the April 3rd, 2017 precipitation event for both the FMCW and NEXRAD radar. The gray curve shows NEXRAD data, while the blue curve is FMCW measured reflectivity and the orange is reflectivity estimated from FMCW DSD estimates. The vertical axis in this plot represents reflectivity in dBZ, while the horizontal is time in hours from the beginning of the event. This plot demonstrates a significant calibration bias between the NEXRAD and FMCW radars. It appears that measured reflectivity data from the FMCW radar data is biased lower than NEXRAD data by 10 to 15 dB across the event. There is some variation in data due to a mismatch in temporal resolution. This seems to suggest the FMCW radar needs an alternate calibration method in rainy conditions.

A rough correction factor may be constructed through comparison with NEXRAD radar data, but a higher resolution calibrated instrument is required to minimize error. Preliminary results applying an approximate correction factor shows promise. Multiplying the 'calibrated' Doppler spectrum by a correction factor of 20 (13dB) shows a similar increase in measured reflectivity factor, as one would expect. Using the same corrected Doppler Spectrum, the bias in estimated reflectivity factor is reduced from 12.5 dB to approximately 5 dB. This is a much more reasonable result- this error is possibly entirely explained by the measurement resolution of the NEXRAD radar, and approximate relations used for calculation.
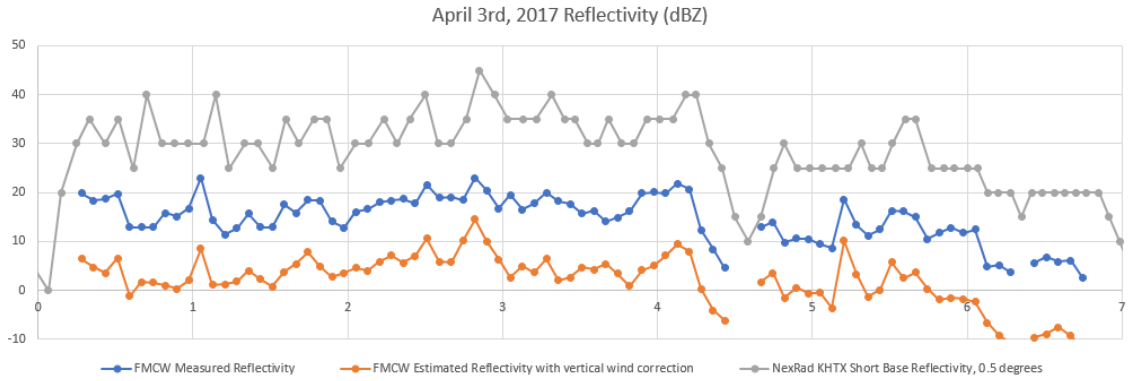
**Figure 6.27.** Comparison of Reflectivity Factor between the UMass FMCW and NEXRad radars.

# CHAPTER 7

# SUMMARY AND CONCLUSIONS

Recent modifications to the UMass FMCW radar have improved measurement capability. System self-interference is mitigated by replacing the original TWT power amplifier with an SSPA, and by driving the analog to digital converter differentially. Increased receiver sample rate makes a higher unambiguous velocity range possible. New data processing hardware and software allows for software controlled adjustment of several nominal system parameters. Trade-offs between parameters such as range resolution, maximum range, FM sweep time, and sweep bandwidth can be dynamically changed. Dynamic range can be adjusted at the time of deployment to increase sensitivity or increase the receiver saturation point.

Improved measurement capability allows for characterization of not only reflectivity and velocity in both clear-air and light to moderate precipitation cases. Improved computational power provides real-time pre-processing and display of preliminary results. Full Doppler Spectral processing and software filtering is performed on the data afterwards. These improvements and increased receiver saturation power make estimates of the Drop Size Distribution possible.

By comparing measured reflectivity factor and reflectivity factor estimated from DSD results, this paper demonstrated an ability to assemble biased drop size distributions. There is significant evidence in the dataset that any vertical winds present will bias results, and these biases can be removed in some cases. When rainfall is light enough that it does not overwhelm signals scattered from turbulent air, wind biases can be directly observed in spectral form. In heavier rains, extraction of wind

biases are not observable with this system. There is strong evidence when comparing the dataset to other instruments that the FMCW calibration during precipitation is not sufficiently to provide accurate results. This is due to the approach of estimating the noise floor value as a median of the Doppler Spectrum; an assumption which does not hold for this instrument in rainy conditions. When the noise floor estimates are too high, they are reset to a value measured with receiver input terminated; this is not sufficient for accurate calibration. It is possible a correction factor can be approximated for this dataset using data collected from a calibrated instrument.

Several improvements could be implemented in this system to improve results in future work. A more effective calibration method would improve precipitation data significantly. Adding a variable or switched attenuator into the system could effectively increase the system dynamic range as needed to mitigate receiver saturation in rain and improve clear-air sensitivity. The data rate could be minimized while maintaining necessary measurement resolution by using a large sweep time in clear-air conditions, and a smaller sweep time in rain. Alternate methods of detecting vertical wind could be used to correct DSD estimates. A co-located disdrometer system could improve these results if the profile has constant velocity, or another radar system with wavelength resonant with drops of specific diameter could show the vertical wind speed versus height.

# APPENDIX

# RADAR OPERATION INFORMATION

This appendix summarizes the operation of the FMCW radar and accompanying hardware.

## A.1    Operation

Before beginning operations, verify that all systems are properly connected together. See next section for details.

Ensure the power switch box is set for the desired source, either generator power or 240. You can bypass this switch box with a 120 V feed, but the roof air conditioner will not run. Power on the system.

To run on generator power, switch the power switch to 'generator'. *Never switch the power switch while either input is powered.* You can start the generator from the 'start' buttons on the generator or on the ceiling by the driver's side door. The generator feeds directly from the gas tanks on the truck via a 'T' connection. To run on 240 V, make sure the power switch is switched to 'Normal'. Then plug in the power.

Log into the computer, Acadia, with user-name 'radarop', and password . Code to run the system is stored in the fmcw directory. fmcw.py is the python file which runs the c++ code to configure the system sweep and start data collection. It also plots the data on the screen. This code saves raw data into the '/data' directory. A new file is created every five minutes. The averaged Doppler spectrum can be viewed in real time using the python code 'plot_fmcw_spectra.py'.

The fmcw parameters can be adjusted by modifying the 'params.txt' file.

Once the data collection starts, if there are no problems, the SSPA can be enabled by pushing the green button on the front. It should illuminate, and the power monitor screen should show the output power. Verify that the receiver is not in saturation by looking at the time domain plot. You can also enable and disable the SSPA through the Ettus I/O. See 'sspa_off.cpp' and 'sspa_on.cpp'.

The processing of raw datafiles is likely to change. This document will not document this process.

## A.2  System Configuration

On the RF box, the labels 'RF IN' and 'RF OUT' should connect to the Receiver antenna and SSPA, respectively. The 'DDS', 'GND' and 'Alarm' cables should connect to the corresponding port on the Ettus box. This ground cable carries the ground of the baseband to the Ettus, and it is important to keep this separate from the chassis ground from an interference perspective. The '+' and '-' ports on each box carry the differential baseband signal to the Ettus. These cables can be switched arbitrarily since they should have the same DC offset, and magnitude. The blue Ethernet cable coming out of the Ettus box is the network connection for the Ettus, and connects to the point labeled 'USRP' on Acadia. Replacement cables should be CAT 5e, slower cables will throttle the data rate. A power cable should connect to the Ettus box and the Power supply box. Finally, there should be a wide multi-conductor cable to bring power from the power supply box to the RF box.

For travel, the antenna feeds need to be removed to prevent damaging the section that holds the feed in focus. This is done by unbolting the large circular disk from the dish and taking it out. Then, unbolt the smaller ring of 6 bolts and slid the feed out through the top. Re-mount the large circular disk onto the dish, to prevent the dish screws from warping. Repeat this process in reverse to put the feed back in.

## A.3 Miscellaneous

1). The truck and generator run on diesel fuel. The truck has a dual fuel tank system, with an imbalance when driving down the highway. It will draw gas from the fuel tank without the gas gauge attached. Do not trust the gas gauge. Manually check the fuel level in both gas tanks and refuel often.

2). The instrument panel on the truck was intermittently "freezing" while driving. The "water in fuel" light also came on occasionally when it was raining. Some connections on the instrument cluster have been re-soldered to mitigate this, and this behavior was not observed afterwards during these deployments.

3). The antenna radomes will tear when driving long distances from flapping in the wind/hitting things (trees). Wrap a strip of packing tape *tightly* around the radome just under the lip of the shroud to prevent this. Also tie something rigid (like cardboard) around areas which show signs of tearing. Take care not to fall.

4). There is an alarm for when the LO clock comes unlocked. It is connected to an input pin on the USRP, and recorded into the raw data files. Monitor this pin to make sure this clock stays locked. It came unlocked several times between deployments.

## A.4 Recommended upgrades

Consider restructuring the power system in the truck, since the 240 V power is not necessary without the TWTA.

Finish construction/implementation of the pedestal controller. Snow/ice will need to be cleared off the pedestal during winter months, tilting the pedestal is easier than climbing on it and sweeping snow off with a push broom.

Data rate was too high during the 2017 experiment to keep up with, and several days of raw data were lost as a result. The easiest way to minimize data rate is

to switch to higher sweep times (low unambiguous velocity range) during clear-air conditions and lower sweep times for precipitation.

It is recommended to better understand the system sidelobe characteristics evident in the Doppler spectrum, and sources of bias in DSD measurements if this system will be used for DSD estimates in the future.

# BIBLIOGRAPHY

[1] Scott A. Mclaughlin, "A new data acquisition system for the u.s. army fm-cw radar: Still a great way to see half-meter resolution," .

[2] Turker Ince and Stephen J. Frasier, "An s-band frequency-modulated continuous-wave boundary layer profiler: Description and initial results," *Radio Science*, vol. 38, pp. 1072, 4 2003.

[3] Merrill I. Skolnik, *Introduction to Radar Systems*, McGraw-Hill, third edition, 2001.

[4] David M. Pozar, *Microwave Engineering*, Wiley, fourth edition, 2012.

[5] Hans Ottersten, "Atmospheric structure and radar backscattering in clear air," *Radio Science*, vol. 4, pp. 1179–1193, December 1969.

[6] John C. Wyngaard, *Turbulence in the Atmosphere*, Cambridge University Press, 2010.

[7] Richard J. Doviak and Dusan S. Zrnic, *Doppler Radar and Weather Observations*, Dover Books, 1993.

[8] D. Atlas, R.C Srivastava, and R.S. Sekhon, "Doppler radar characteristics of precipitation at vertical incidence," *Reviews of Geophysics and Space Physics*, vol. 11, pp. 1–35, February 1973.

[9] Turker Ince, *Clear-Air Radar Observations of the Atmospheric Boundary Layer*, Ph.D. thesis, University of Massachusetts, Amherst, 2001.

[10] J. S. Marshall and W. McK. Plamer, "The distribution of raindrops with size," 1948.